Lattice Dynamics of Hybrid Halide Perovskite Single Crystals by Dielectric Spectroscopy

GIANNIS G. GKIKAS



Heraklion Crete, Sept. 2022

Περίληψη

Οι περοβσκίτες αναφέρονται σε μια κατηγορία υλικών που έχουν κερδίσει σημαντική προσοχή στον τομέα της οπτοηλεκτρονικής και της τεχνολογίας ηλιακών κυττάρων. Κυρίως αποτελούμενες από οκταέδρα μετάλλου αλογόνου που περιβάλλει ένα κεντρικό κατιόν, αυτά τα υλικά εμφανίζουν συχνά μοναδικές δομικές, ηλεκτρονικές και οπτικές ιδιότητες. Οι περισσότερες εκ των χαλιδικών περοβσκιτών που έχουν μελετηθεί εκτενώς για τις εντυπωσιακές τους φωτοβολταϊκές ικανότητες βασίζονται σε μόλυβδο και εμφανίζουν κρυσταλλική δομή περοβσκίτη.

Η έρευνα πάνω στις χαλιδικές περοβσκίτες έχει επιταχυνθεί λόγω των εξαιρετικών τους ιδιοτήτων απορρόφησης φωτός και μεταφοράς φορτίου, οδηγώντας σε εντυπωσιακές προόδους στην αποδοτικότητα των φωτοβολταϊκών κυττάρων περοβσκίτη. Η ευελιξία των χαλιδικών περοβσκιτών εκτείνεται πέρα από τη φωτοβολταϊκή, καλύπτοντας εφαρμογές σε Light Emitting Diodes (LEDs), lasers και φωτοανιχνευτές.

Καθώς η παρούσα μεταπτυχιακή εργασία εστιάζει στον δηιλεκτρικό χαρακτηρισμό με σκοπό την μελέτη της δομής επί την επίδραση ηλεκτρικού πεδίου.

Acknowledgments

I would like to express my gratitude to my supervisors, **Alexandros Lappas** and **Constantinos Stoumpos** for letting me being part in both research groups. Being there for all my questions. Providing me satisfaction, as having the opportunity to grow the single crystals and study their properties.

I would like also to thank **Emmanouel Kymakis** from the Hellenic Mediterranean University, being part of my committee.

Finally, I would like to thank all the members of both research groups that I have worked with at **Quantum Materials & Magnetism** at Institute of Electronic Structure and Laser-Foundation for Research and Technology - Hellas and **Crystal Chemistry Laboratory** at the University of Crete.

Table Of Contents

Cover 1

Περίληψη 2

Acknowledgments 3

Abstract 5

1. Introduction 6

1.1 Perovskites 6

1.2 Dielectric &Optoelectronic Properties 9

2. Experimental 18

2.1 Materials 18

2.2 Syntheses 19

2.3 Crystal Growth 20

2.4 Powder X-ray Diffraction 22

2.5 Optical Characterization 24

2.6 Dielectric Spectroscopy 25

2.6.1 Magneto-Dielectric Custom-Made Station 25

2.6.2 Structural Dynamics & Phase Transitions 27

3. Results and Discussion 31

3.1 Dielectric permittivity & Lattice Dynamics 31

3.2 Dielectric Properties Versus Frequency 34

4. Analysis 39

5. Conclusions and Perspective 43

6. Literature 44

Abstract

Halide perovskites AMX_3 (A^+ = Cs, CH_3NH_3 or $HC(NH_2)_2$, M^{2+} = Pb, Sn or Ge and X^- = Cl, Br or I), are amongst the leading emerging materials in the past decade towards optoelectronic and environmental remediation applications, including devices such as solar cells, light-emitting diodes, hard radiation detectors and photocatalytic modules. What makes these semiconductor materials so attractive for optoelectronic devices is their superb absorption across the visible and near-infrared region (E_g = 1.1-3.0 eV) and their high charge-carrier mobility and long charge-carrier diffusion lengths. An important research branch of halide perovskites focuses in the understanding of the underlying physicochemical origins of these fascinating properties, which is currently lacking. Such understanding will be beneficial not only from the fundamental science perspective but also crucial for the rational enhancement of the optoelectronic performance.

In this work, mm-sized single-crystals of hybrid halide perovskites were grown ($MAPbCl_3$ and $MAPbBr_3$) and studied. Structurally and spectroscopically using a custom made set up, with capabilities to investigate the lattice dynamic of the crystalline material, and correlate the phase transition transformation to the dielectric properties. Also, relaxation time mechanisms were studied compering different models and proving the optional as the Havriliak-Negami. Calculated the relaxation time and the exponents of the fitting model, providing information of the dipole behavior.

1.Introduction

1.1 Perovskites

Perovskites were discovered by Gustav Rose in 1839 and where named after Lev Perovski who was the founder of the Russian Geographical Society, in the form of $CaTiO_3$[1]. The mineral is a double oxide of calcium and titanium were the Ti^{+4} cation is coordinated with the O^{-2} anions forming octahedrals $[TiO_6]^{-2}$ and the Ca^{+2} cation is caged between the octahedrals which are corner shared. Since then, a vast majority of ABO_3 was studied with different A and B site cations breaking through the field of energy application such as photochromic, electrochromic, image storage, catalytic, ferroelectric e.t.c [2]. As the field was expanding, a new era for the perovskites began, in 1893 the first halide perovskite was introduced $CsPbX_3$ [3], while methylammonium based lead halide perovskites were reported first time 1978 by Weber [4] and the analogous formamidinium cation was discovered by Stoumpos [5] (D. Mitzi [6] reported the Sn analogue in 1998). The novelty of hybrid halide perovskites was proposed by Miyasaka[7] who have studied the methylammonium halide perovskites as light-absorbing materials as photovoltaics in 2009. Hence the scientific community plunged into these materials due their superb properties, such as a high-absorption coefficient, a long diffusion length, superior charge-transport and solution processability. As result the device performance of photovoltaics has reached form the initial 3.8% to 25.5% within a decade Figure. 1 [8].

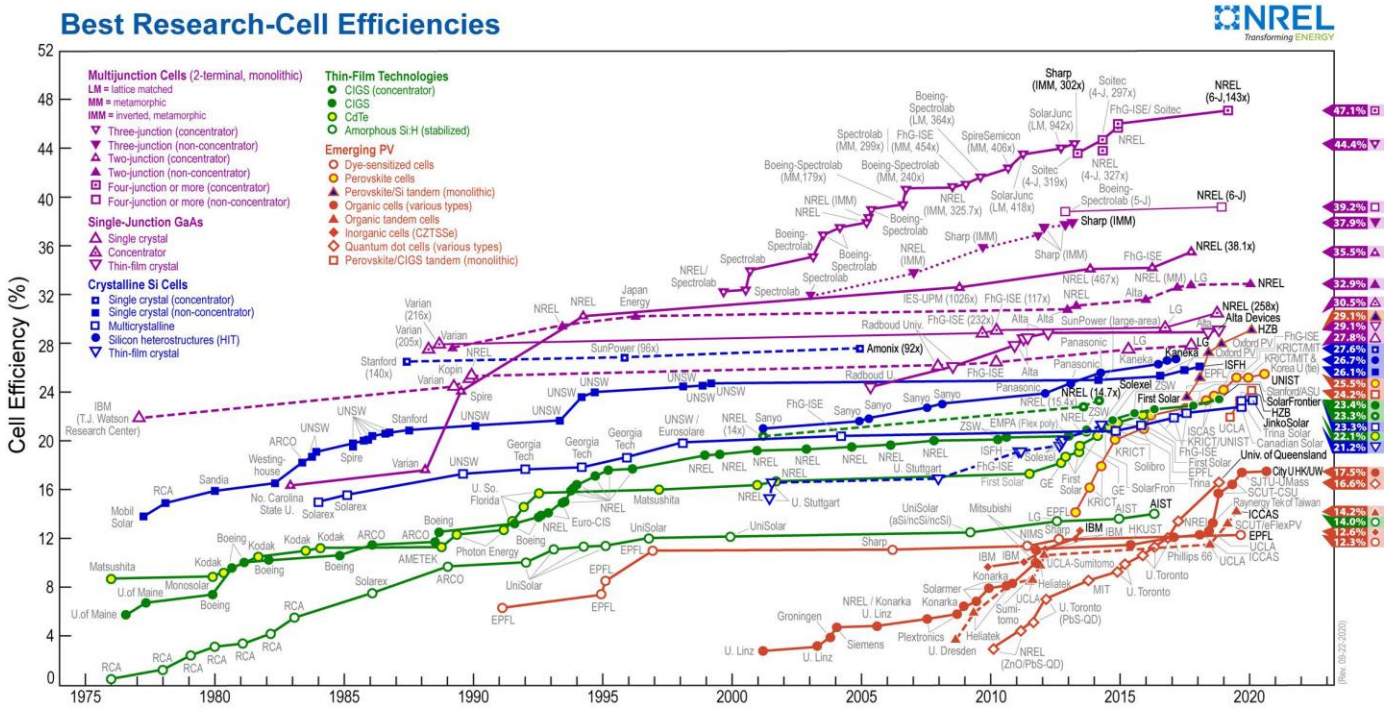


Figure 1. Timeline of research solar cell energy conversion efficiencies (National Renewable Energy Laboratory) [8].

These materials are quite impressive due to their crystal-structure and how the deviation from the ideal cubic structure Pm3m [9] (Fig. 2) can tune the optoelectronic properties via lattice strain and transformation to other crystal structures. Also, an interesting behavior is how the chemical substitutions can affect the properties of these materials, such as the band-gap (Fig. 3) [10]. As thus, it is important to investigate the lattice dynamics and the crystal structure due to the correlation with a plethora of optoelectronic properties.

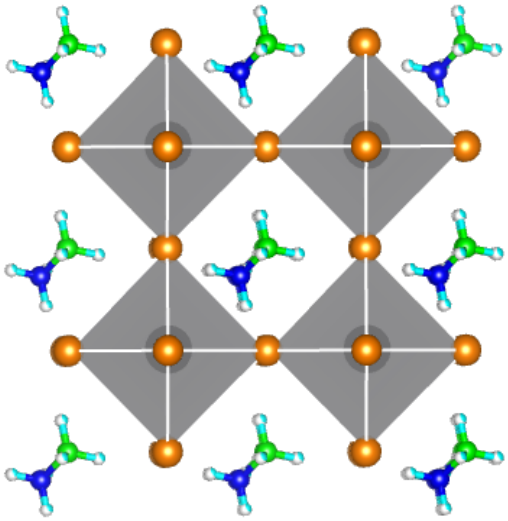


Figure 2. Ideal Cubic Crystal Structure of $CH_3NH_3PbBr_3$. Orange atoms refer to Br, grey to Pb, green to C, navy N and white-blue to H.

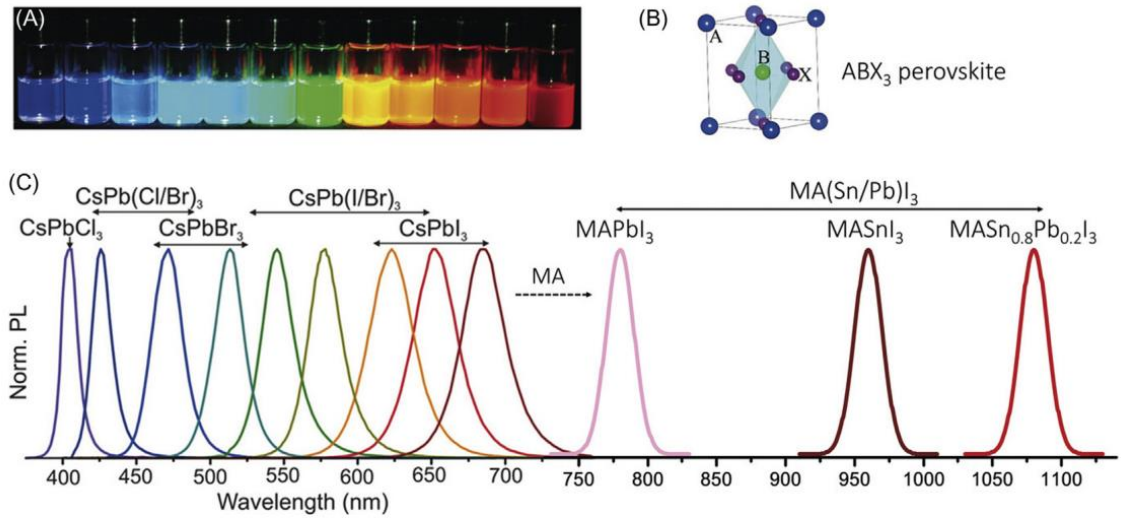


Figure 3. Band gap tunability for ABX_3 strustures ranging from 1.15 eV to 3.06 eV. a) colloidal solutions of nanocrystals under UV light. b) generic crystal structure of ABX_3 perovskite. c) Representation of PL spectra of the halide colloidal solutions [10].

1.2 Dielectric &Optoelectronic Properties

Metal Halide Perovskites have been discussed quit a lot on their unusual ferroic properties that are generally absent in classical photovoltaics. In particular, a debate on the presence of ferroelectricity has been discussed for several years [11]. Ferroelectric materials are dielectric materials in which have spontaneous electric polarization and can be reversed by the application of an external electric field. These phenomena take place only below a certain phase transition temperature the Curie temperature, T_c and above this temperature the spontaneous polarization vanishes as the crystal transforms into the paraelectric state.

Ferroelectricity can occur in two different type of phase transitions, the displacive and the order-disorder. In the displacive phase transition Figure 4 a) the ion is displaced from the equilibrium as thus this leads to the orientation of the permanent dipole moment. $NaNO_2$ is classified as one of the most typical ferroelectrics with order-disorder type, where the NO_2^- is treated as the order-disorder unit [12]. For $BaTiO_3$ the displacive transition occurs when the B site ion, titanium is slightly displaced within the oxygen octahedra [13]. The order-disorder transition Figure 4 b), there is a dipole moment in each unit cell and are temperature dependent. Also a mixed state can be achieved, where both kinds of transformation may take place and this is the ferroelectric mechanism which is proposed for the , three dimensional halide perovskites Figure 4 c) [14].

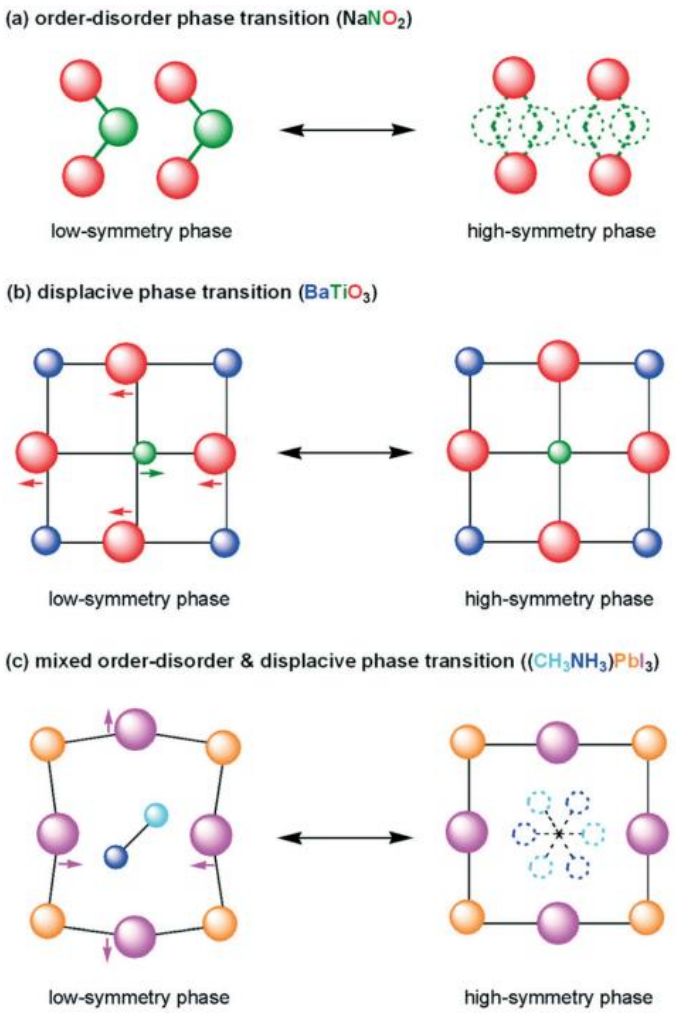


Figure 4. Schematic illustration of the phase transition mechanism in ferroelectrics. a) order-disorder type, b) displacive type, and c) mixed order-disorder & displacive type [14].

To get a first glimpse of ferroelectricity is the study of the permittivity, where permittivity is a measure of the electric polarizability of a dielectric. It is dependent on the structure and its evolution with T as well as it response to stimuli, such as the E field or other extrinsic paramters. The following equation is the permittivity (eq. 1) were ε_r is relative permittivity, ε_0 is vacuum permittivity (~$8.854 \cdot 10^{-12}$ F/m), χ is electric susceptibility:

$$\varepsilon=\varepsilon_r\cdot\varepsilon_0=(1+\chi)\cdot\varepsilon_0 \qquad [1]$$

The electric displacement field D (eq. 2), is defined as how an electric field E influences the organization of electrical charges in a given medium, inducing charge migration and electric dipole reorientation, where D is related to charge densities and E is related to the forces and the potential differences:

$$D=\varepsilon\cdot E \qquad [2]$$

The polarization P (eq. 3), is defined as the displacement of bound charged element present to an external electric field. The positive charged elements displaced in the direction of the field, and the negative charged elements are displaced opposite to the direction of the field. The molecules may remain neutral in charge, yet an electric dipole moment forms.

$$P=\varepsilon_0\cdot\chi\cdot E \qquad [3]$$

Dielectric materials respond in different ways to the applied electric field, E. In linear dielectrics the induced polarization is proportional to the electric field, in paraelectric phases the material is polarized nder the applied electric field, ferroelectric materials have spontaneous electric polarization that can be reversed by the application of an external electric field, relaxor ferroelectrics resemble nonlinear paraelectrics and antiferroelectric materials have a line of ions which are spontaneously polarized and a neighboring line polarized in antiparallel direction Figure. 5 [15].

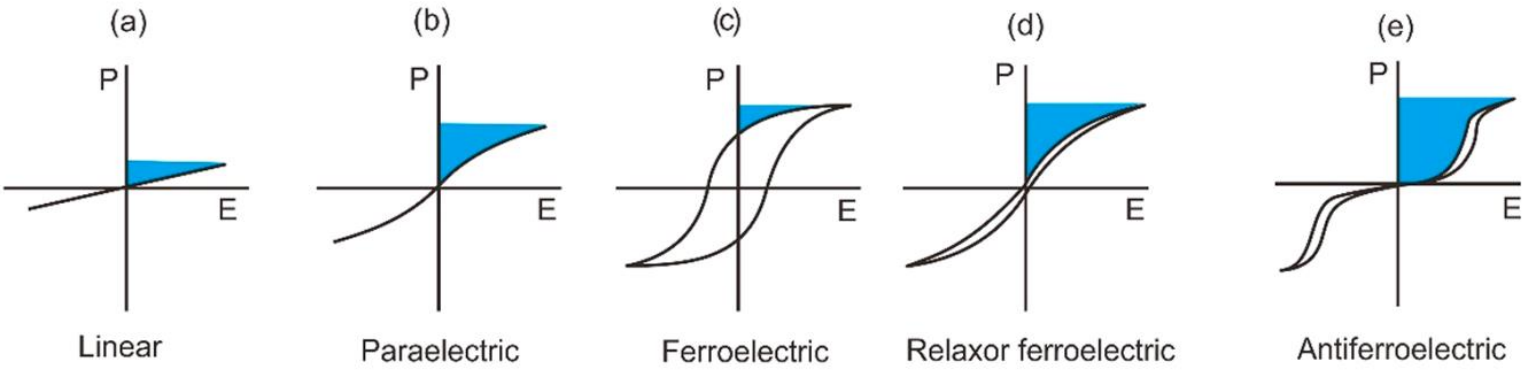


Figure 5. Polarization-electric field curves of several types of dielectric materials the blue area above the curve represents the energy storage density of each material. P represents the polarization of the material, and E represents the applied electric field [15].

The relative permittivity is a complex function (eq. 4), where ε′ is the real part and represents the energy stored and ε′′ is the imaginary part that represents the dielectric losses. The tanδ (eq. 5) represents the non-ideal circuit of a linear connected capacitor in an AC circuit Figure. 6 [16] and the capacitance (eq. 6) is defined as the area A of two parallel plates separated by a distance d and with the dielectric constant of the capacitor ε .

$$\varepsilon=\varepsilon' - i\varepsilon'' \qquad [4]$$

$$\tan\delta=\varepsilon''/\varepsilon' \qquad [5]$$

$$C=\varepsilon'\cdot\varepsilon_o\cdot A/d \qquad [6]$$

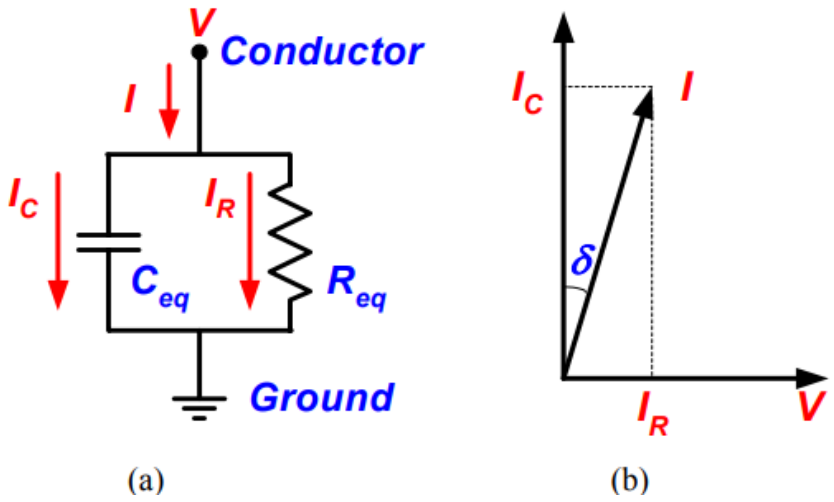


Figure 6. a) electric circuit of a non-ideal capacitor, b) phasor diagram representation of capacitive and resistive currents [16].

A different approach to investigate similar phenomena with the dielectric permittivity is the electrical modulus (eq. 7) [17]. The electrical modulus physically corresponds to the relaxation of the electric field in the material and as a result it represents the real dielectric relaxation process. The modulus M* is defined as inversely proportional to the permittivity of the material and represents the relaxation of the electric field within the DUT (device under test).

$$M=M'+jM'' \quad [7]$$

Broad band dielectric spectroscopy is a direct measurement of the electrical and structural properties of a material applying a stimuli to the sample. Via different frequency-dependent techniques, such as alternating electric field, radiofrequency microwave and pulsed laser pump and probe, the dielectric function can be uncovered for different processes Figure. 7 [18].

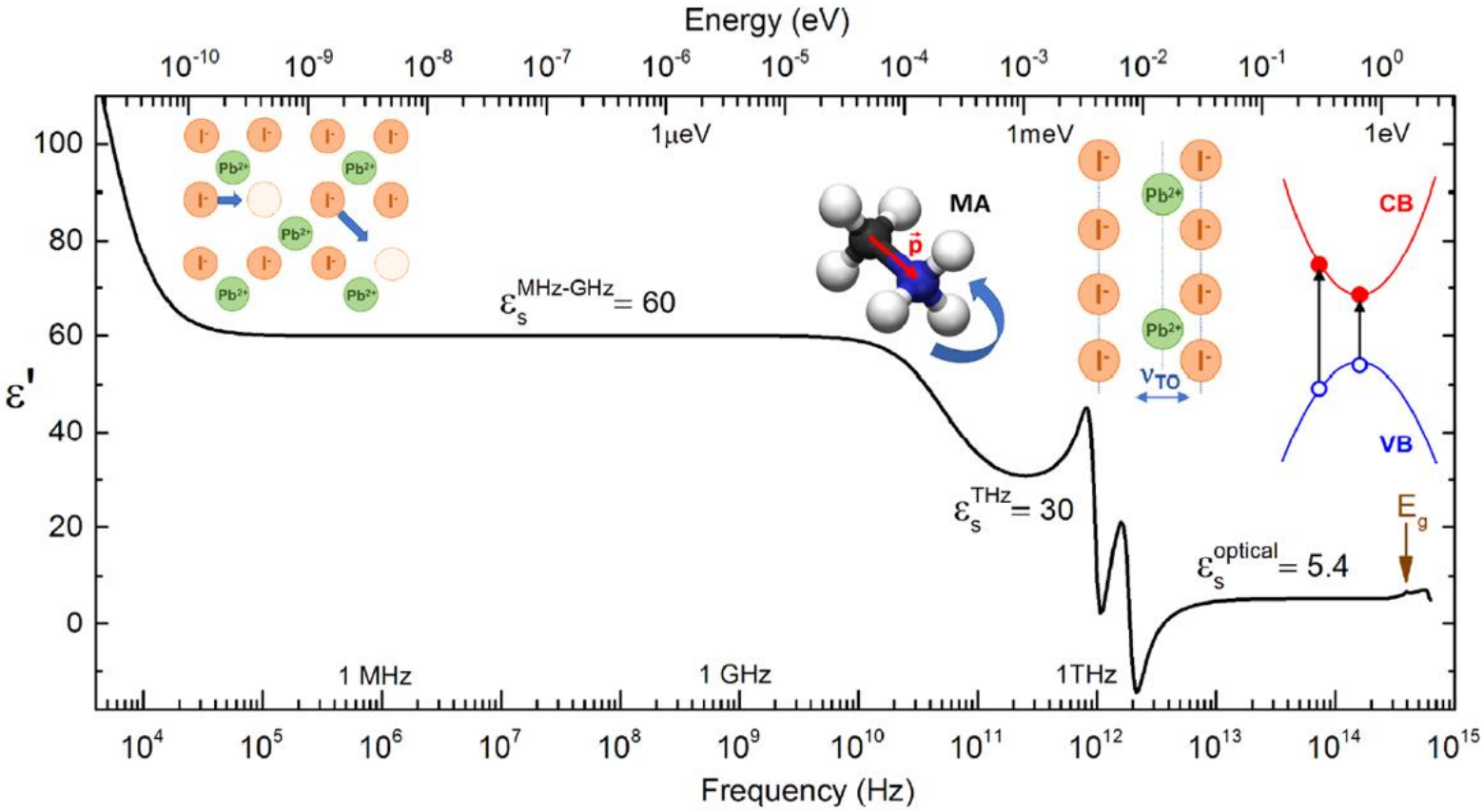


Figure 7. Schematic representation of the frequency-dependent relative permittivity of $MAPbI_3$ at room temperature at different frequency domains [18].

The dielectric mechanisms which take place are related into characteristic frequency region. From the high frequency region (~10^{15} Hz) the electronic polarization takes place as the electronic density is displaced, at THz region (10^{12} Hz) atomic polarization is observed when the nucleus of the atom reorients in response to the electric field, at region 10^{10} Hz the dipoles relaxation is observed as the dipoles tend to slightly reorientate and at 10^{10} Hz to low frequencies the ionic and dielectric relaxation takes place. The ionic relaxation appears due to the trap of charge carriers at interface or any type of space charge losses and the dielectric relaxation represents the movement of the dipoles and electric charges.

In this thesis, the focus was in the investigation of the contribution of the various structural phase transitions to the dielectric permittivity and the dielectric relaxation function by attempting to quantify the relaxation times via the Debye expression (eq. 8, 9). Debye theory (1912), assumes that the molecules are spherical in shape and dipoles are with only one relaxation time and no interaction between of the dipoles. Where τ is the relaxation time, ε_∞ (high-frequency limit), ε_s (low frequency, static limit) and ω is the angular frequency $\omega=2\pi f$.

$$\varepsilon'(\omega) = \varepsilon_\infty + \frac{\varepsilon_s - \varepsilon_\infty}{1+\omega^2\tau^2} \qquad [8]$$

$$\varepsilon''(\omega) = \frac{(\varepsilon_s - \varepsilon_\infty)\omega\tau}{1+\omega^2\tau^2} \qquad [9]$$

Since the Debye expression cannot properly predict the behavior of some liquids and solids, in 1941 Cole K.S. and Cole R.H. proposed an improved description, known as the Cole-Cole equation (eq. 10):

$$\hat{\varepsilon} = \varepsilon_\infty + \frac{\varepsilon_s - \varepsilon_\infty}{1+(i\omega\tau)^{1-\alpha}} \qquad [10]$$

Where, α is a constant for a given material, having a value between $0 \leq \alpha \leq 1$, and $\alpha=1$ represents the Debye relaxation limit while in the case of $0 < \alpha$, the relaxation is stretched and extends in higher frequency range than the previous model. Ten years later, in 1951, Davidson (eq. 11) et al., proposed the following expression (Cole-Davidson equation) to interpret data observed on propylene glycol and glycerol[19] :

$$\hat{\varepsilon} = \varepsilon_\infty + \frac{\varepsilon_s - \varepsilon_\infty}{(1+i\omega\tau)^\beta} \qquad [11]$$

Here β is a constant for a given material, having value $0 \leq \beta \leq 1$, where β=1 represents the Debye relaxation limit and in the case of $\beta < 1$ the model represents similarly to the Cole-Davidson, the extended broadening in higher frequencies, also indicating the temperature dependence of the relaxation mechanisms, while as the value of β decreases, the larger the distribution of relaxation time takes place. Both the Cole-Cole and Cole-Davidson equations were empirical and could be considered to be the consequence of the existence of a distribution of relaxation times rather than that of a single relaxation time (Debye equation). After 15 years, in 1966, S. Havriliak and S. J. Negami, combined the Cole-Cole and Cole-Davidson equations for polymers. The Havriliak-Negami equation (eq. 12) becomes:

$$\hat{\varepsilon} = \varepsilon_{\infty} + \frac{\varepsilon_s - \varepsilon_{\infty}}{(1+(i\omega\tau)^{1-a})^{\beta}} \qquad [12]$$

The above equation has two distribution parameters, α and β obtaining values of $0 \leq \alpha \leq 1$, and $0 \leq \beta \leq 1$.

Valuable insights for the above models can be derived by plotting the imaginary part of the dielectric permittivity, at y-axis and the real part of the permittivity, at x- axis, which depicts as a semicircle, connecting the ε_{∞} (high-frequency limit) to ε_s (low frequency, static limit) on the real axis permittivity and allows for the evaluation of the distribution factors Figure. 8 [20].

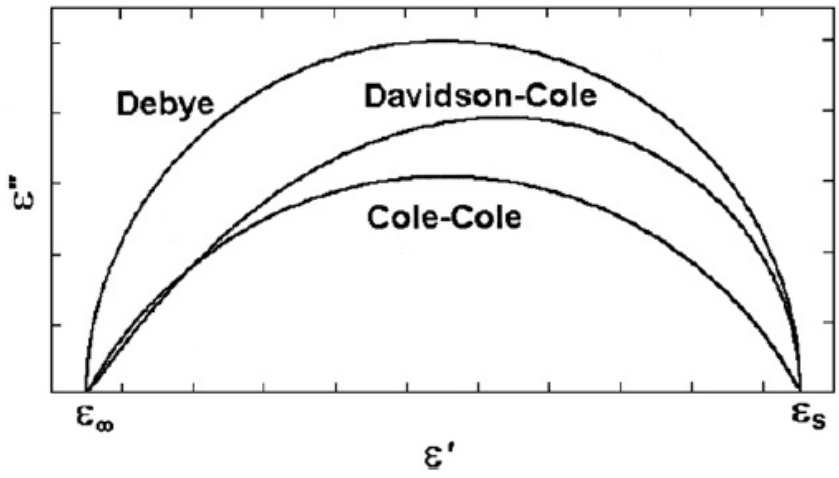


Figure 8. Schematic representation of the semicircle plot of the imaginary part versus the real part of the dielectric permittivity for the different models compering the distribution factors [20].

Moreover, the argand diagrams Figure. 9 [20] allow to represent the ε′ and ε′′ versus the frequency, ω based on the various relaxation models. The mathematical expressions can predict the mechanism, which is responsible for the dielectric losses via the symmetric broadening and the relaxation time.

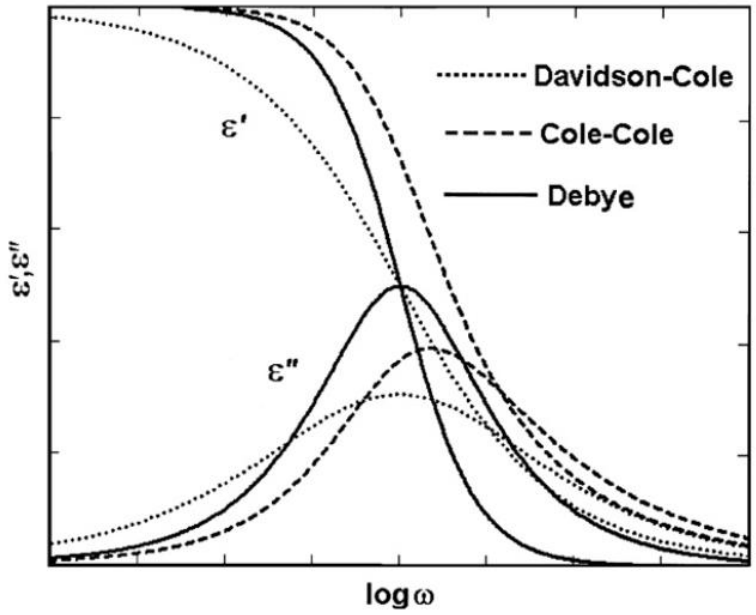


Figure 9. Schematic representation of the real and imaginary part of the dielectric permittivity versus the frequency of the alternating electric field for the different derivatives of the Debye model (eq. 8 to eq. 12) [20].

2. Experimental

2.1 Materials

Reagents for chemical synthesis were purchased from:

(a) Sigma-Aldrich: HBr (48% w/w in H_2O), HCl (37% w/w in H_2O) (, N-N Dimethylformamide (DMF) (99.8%), Dimethyl sulfoxide (DMSO) (99.7%), CH_3NH_2 (40% w/w in H_2O), methylammonium chloride (CH_3NH_3Cl).

(b) Supelco: $Pb(NO_3)_2$ (98%), $PbCl_2$ (99%) and KBr (99%).

Chemicals for preparation of specimens for dielectric measurements were purchased from:
(a) Ted Pella: Conductive Gold Paste, Conductive Silver Paste, Conductive Carbon Paste and SEM Gold/Silver Extender.

(b) Goodfellow: Gold (Au) Wire of 25 μm diameter and length 10 m

$PbBr_2$, CH_3NH_3Br and CH_3NH_3Cl were synthesized according to the following protocols.

2.2 Syntheses

CH_3NH_3Br: 11.49 mL (100 mmol) of aqueous 48% w/w HBr solution and excess 17.32 mL (200 mmol) of CH_3NH_2 are mixed slowly into a 100 mL beaker in an exothermic reaction to produce a clear, colorless solution. The solution was heated until the remnant water was evaporated. The thus obtained colorless CH_3NH_3Br solid was collected, transferred to a 20 mL scintillation vial and dried overnight at 85 °C under vacuum. Yield 90% (10.08 g).

$$CH_3NH_2 + HBr \longrightarrow CH_3NH_3Br$$

CH_3NH_3Cl: 8.33 mL (100 mmol) of aqueous 37% w/w HCl solution and excess 17.32 mL (200 mmol) of CH_3NH_2 are mixed slowly into a 100 mL beaker in an exothermic reaction to produce a clear, colorless solution. The solution was heated until the remnant water was evaporated. The thus obtained colorless CH_3NH_3Cl solid was collected, transferred to a 20 mL scintillation vial and dried overnight at 85 °C under vacuum. Yield 93% (6.279 g).

$$CH_3NH_2 + HCl \longrightarrow CH_3NH_3Cl$$

$PbBr_2$: was prepared by mixing aqueous solutions of $Pb(NO_3)_2$, dissolved in 200 mL of H_2O, and KBr dissolved in 400 mL of H_2O, in 1:2 molar ratio under vigorous stirring. Upon mixing, a white voluminous solid immediately precipitates. The stirring is continued for a further 5 minutes and then left to stand for 15 minutes, during which time the solid settles at the bottom of the reaction beaker. The solution was filtered under water pump generated vacuum and the white $PbBr_2$ which was obtained was transferred to four different petrit dishes and dried overnight at 85 °C under vacuum. Yield 94% (344.99 g), Figure. 10.

$$Pb(NO_3)_2 + 2KBr \longrightarrow PbBr_2 + 2KNO_3$$

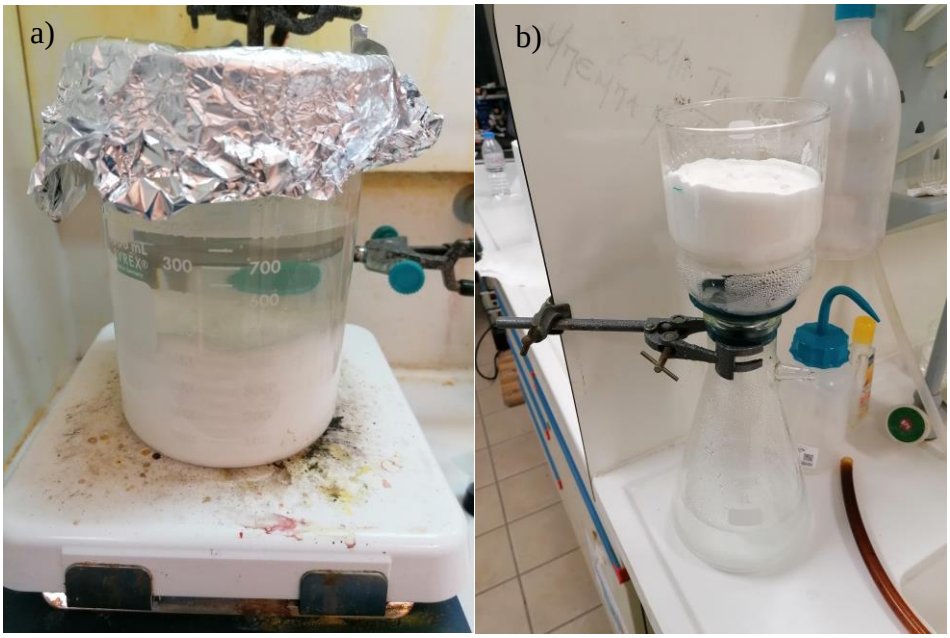


Figure 10. a) $PbBr_2$ solution under stirring, b) filtering of $PbBr_2$ solution.

2.3 Crystal Growth

The crystal growth methodology of halide perovskites which was applied involves the so-called Inverse Temperature Crystallization (ITC), which was proposed by Bakr et al. [21] Figure 11. This process takes advantage of the anomalous decrease in the solubility of the perovskites with increasing temperature in polar organic solvents, such as N,N-Dimethylformamide (DMF) and Dimethyl Sulfoxide (DMSO). Due to this uncommon property, large perovskite single crystals can be grown at an elevated temperature in a short period of time (typically few hours).

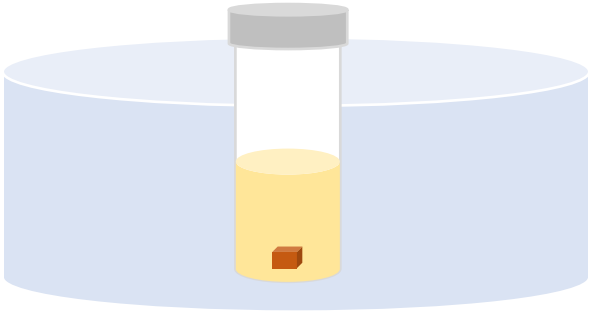


Figure 11. Schematic illustration of the Inverse Temperature Crystallization (ITC) technique. [20]

$CH_3NH_3PbBr_3$: a nearly saturated methylammonium lead bromide solution was prepared by dissolving 10mmol of $PbBr_2$ and 10mmol of CH_3NH_3Br into 10 mL of anhydrous DMF in a 20 mL scintillation vial. The solution was filtered at room temperature using a 45 μm PTFE filter and placed in a thermostated oil bath. Single-crystal of the compounds were grown via the inverse temperature crystallization (ITC) method Figure 12. Briefly, the clear solution was placed in a pre-heat silicon oil bath at 78 °C and the solution was left standing for 3 hours. Large crystals (2.5 x 2.5 x 1 mm^3) of $CH_3NH_3PbBr_3$ were grown. The crystals were isolated by decanting the supernatant solution, placed on a filtration paper (Whatman #1) and pressed dry until no solvent traces could be detected on the filtration paper.

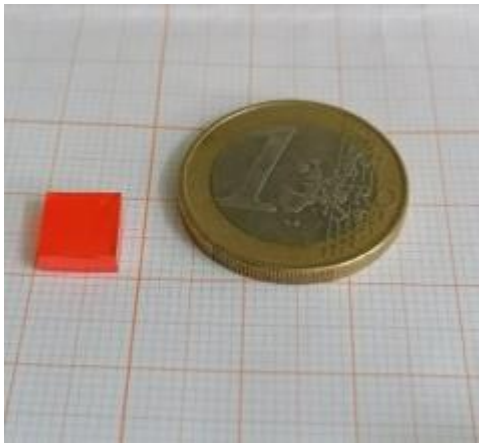


Figure 12. Single crystal of $CH_3NH_3PbBr_3$.

$CH_3NH_3PbCl_3$: a nearly saturated methylammonium lead chloride solution was prepared by dissolving 7.5 mmol of $PbCl_2$ and 7.5 mmol of CH_3NH_3Cl into 10 mL of anhydrous DMF/DMSO (1:1 v/v) in a 20 mL scintillation vial. The solution was filtered at room temperature using a 45 μm PTFE filter and placed in a thermostated oil bath. Single-crystal of the compounds were grown via the inverse temperature crystallization (ITC) method Figure 13. Briefly, the clear solution was placed in a pre-heat silicon oil bath at 68 °C.

After 3 hours, large crystals (2 x 2 x 1 mm^3) of $CH_3NH_3PbCl_3$ were grown. The crystals were isolated by decanting the supernatant solution, placed on a filtration paper (Whatman #1) and pressed dry until no solvent traces could be detected on the filtration paper.

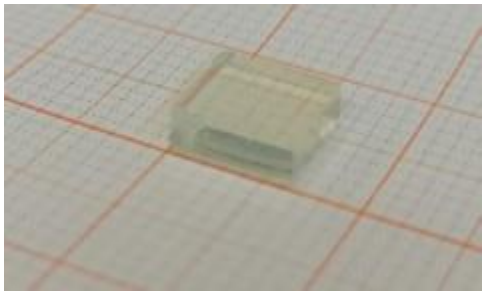


Figure 13. Single crystal of $CH_3NH_3PbCl_3$.

2.4 Powder X-ray Diffraction

Powder X-ray Diffraction (pXRD): X-ray diffraction on pulverized single crystals was collected on a Bruker D8 Advance instrument, at room temperature, equipped with a CuKa X-ray source (λ = 1.5406 Å) operating at 40 kV and 40 mA and a LynxEye Detector, using the Bragg-Brentano measuring geometry, between the 2θ range 5-60º, and a 2θ step size of 0.02º. The collected data were refined using the LeBail method with the crystallographic software JANA2006 [22].

From the LeBail refinements we verified the purity of the single crystals and determined the symmetry of the crystal structure, which is in agreement within the literature of $MAPbCl_3$ [23] and $MAPbBr_3$ [24]. The space group of $MAPbCl_3$ is $Pm\bar{3}m$ (221), cell parameters a=b=c=5.6824(2) Å α=β=γ=90 º , GOF=1.22 and R_w= 19.56 % Figure 14. Similarly, the crystal structure of $MAPbBr_3$ is consistent with the $Pm\bar{3}m$ (221) symmetry, with cell parameters a=b=c=5.9922(2) Å α=β=γ=90 º, GOF=1.68 and R_w= 13.84 % Figure 15.

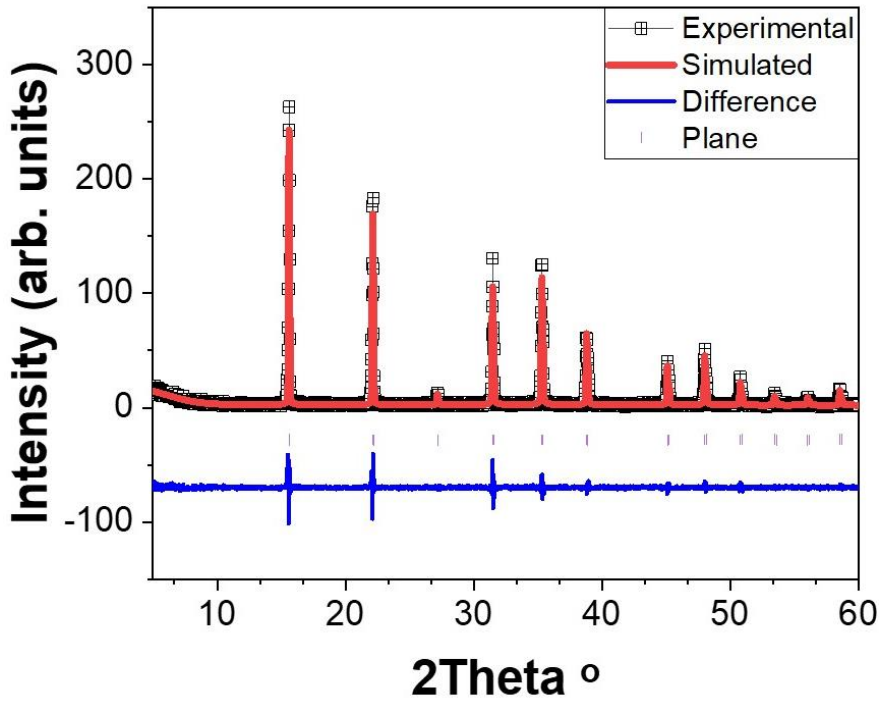


Figure 14. LeBail refinement of powder X-ray diffraction data of $MAPbCl_3$.

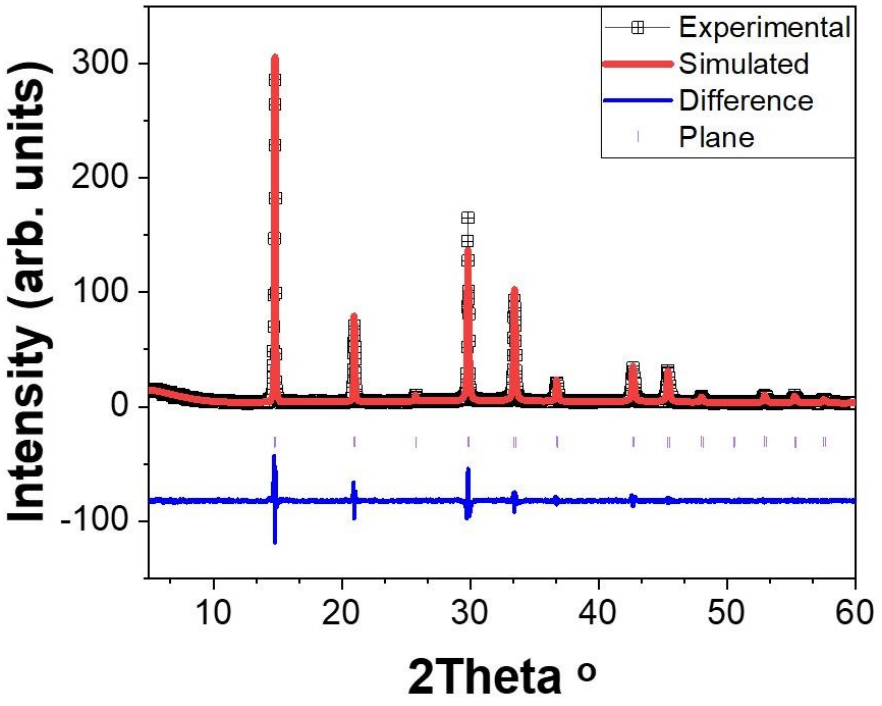


Figure 15. LeBail refinement of powder X-ray diffraction data of $MAPbBr_3$.

2.5 Optical Characterization

Diffuse Reflectance (UV-VIS-NIR): Diffuse reflectance spectra were collected on a Shimadzu UV2600 Plus spectrometer, equipped with an integrating sphere, in the 185-1400 nm spectral range. The sample was placed on top of a $BaSO_4$ "mirror" which was used as the 100% reflectance reference. The obtained spectrum was converted to absorbance using the Kubelka-Munk function (eq. 13) [25].

$$\frac{k}{s} = \frac{(1-R_\infty)^2}{R_\infty} \qquad [13]$$

For $MAPbCl_3$ Figure 16 a) we observe the band-gap at 3.02 eV and the exciton at 2.8 eV (*****) , at the range of 2.75 - 2.25 eV (V) a second slope appears due to vacancies of the X-site anion (chloride) . At 1 eV we can also observe the vibration due to the C-N stretching mode combos and overtones of the methylammonium cation. As for the $MAPbBr_3$ Figure. 16 b) we observe the energy-gap at 2.28 eV and the exciton at 2.4 eV (*). At 1 eV we can also observe the vibration due to the C-N stretching mode combos and overtones of the methylammonium cation.

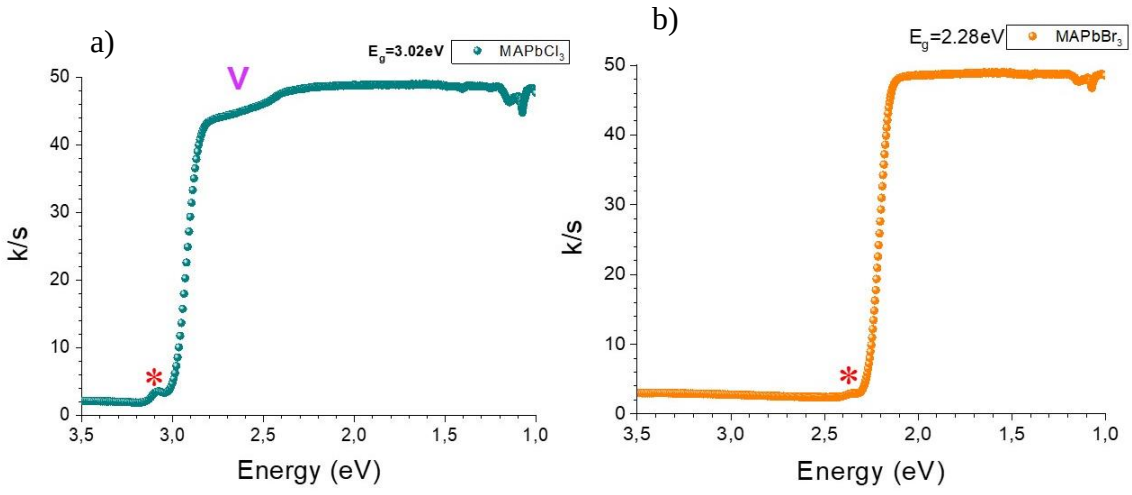


Figure 16. Plot of the absorbance using the Kubelka-Munk model, a) $MAPbCl_3$, b) $MAPbBr_3$.

2.6 Dielectric Spectroscopy

2.6.1 Magneto-Dielectric Custom-Made Station

Dielectric & Dynamic Measurements: The dielectric measurements were collected in the in house Magnetodielectric Station of the Quantum Materials & Magnetism Laboratory at IESL-FORTH Figure 17 [14]. The custom-made system is capable to probe low temperature (LN_2 or LHe) and frequency dependent phenomena with externally applied magnetic or electric stimuli and measure physical quantities like Capacitance and Dielectric Loss, Voltage, Electric DC Current and Impedance. For the purpose of the Capacitance measurements, a precession LCR meter E4980A of Agilent was used with a frequency range of 20 Hz – 2 MHz. Depending on the sample a 4-probe or 2-probe connection can be established and a standard correction can be made depending on the length of the wires/cables used. The temperature of the sample itself and that of the continuous flow cryostat (Janis Research co.) are varied by a Lakeshore 332 temperature controller through a two-loop control, where the channel A is connected with the Cryostat heater, of 40 Ohm and a CX-1050-SD Cernox #X235263 thermometer and the channel B is



Figure 17. Setup of the Magneto-Dielectric Custom-Made Station.

connected with the heater of 20 Ohm, placed on the sample holder stick and a second CX-1050-CU Cernox #X94732 thermometer.

The magneto-electric (MD; Figure 18) probe used in this set up is also home-made system, designed for two different sample carriers, in such way that they can be detached from the main stick and the sample can be mounted on the working bench. The stick is capable to measure dielectric properties (capacitance), resistivity, pyroelectric current and polarization in polycrystalline as well as single crystal sample forms.

.



Figure 18. The home-made carbon fiber stick which is used as sample insert into the cryostat.

The connections of the used instruments and the probe is via BNC connectors since low conductor resistance is a prime consideration for measuring low signals for LCR measurements. The configuration which was applied is the 4-Terminal-Points, since the main probing instrument provides 4 terminals (H_P, L_P, H_C, L_C) and there is also a floating ground (GND), while all 4 wires are connected together on a RF noise shield (copper plate), which is close to the DUT at the back side of the lower carrier socket, in order to limit the stray capacitance that develops among the 4 leads.

In our case, $MAPbX_3$ (X= Cl^-, Br^-) single crystals, were painted uniformly with the conductive Gold Paste at the (100) and (001) parallel crystal facets and gold wires (diameter 25 μm) were attached (with Au paste) at both surfaces. The loose end of the micron thick Au wires, were then attached with tin (Sn-Pb) soldering on the metal pins of the carrier, with the bottom surface of the crystal thermally (with Au paste) anchored on a sapphire substrate, glued with GE varnish onto the holder itself (JIG) Figure 19.

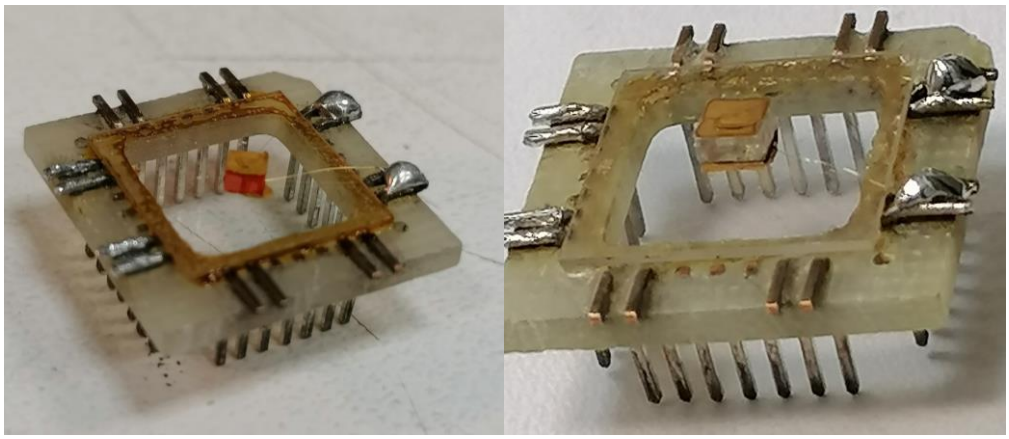


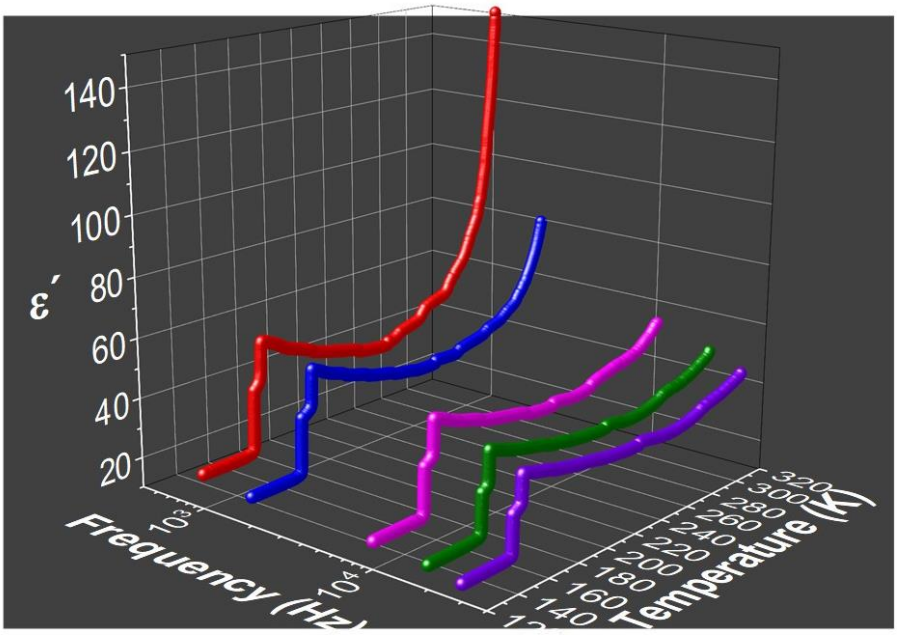
Figure 19. $MAPbX_3$ (X: Cl^-, Br^-) single crystals, gold painted and mounted onto the JIG holder.

2.6.2 Structural Dynamics & Phase Transitions

The structure mediated dynamics of the organometallic halide perovskites was studied through the real and the imaginary parts of the dielectric permittivity. All the measurements were carried via a cooling protocol, with a rate of 0.5 K/min, from 120-320 K, using the LCR Agilent E4980A as electric field stimulation.

$MAPbBr_3$ measured with an applied electric field 1 kV/m and within the frequency range 20 Hz to 30.02 kHz, the data were collected with a sweep profile with no delay between each measured point despite the 600 sec initial delay for the purpose of charging electrically homogenous the sample. For the $MAPbCl_3$ it was necessary to lower the applied electric field to 0.5 kV/m, due to field-driven cracks developed on the measured specimen. Also, a delay was introduced of 20 sec in each measured data and the initial delay of the 600 sec was maintained.

In the case of $MAPbBr_3$ Figure 20, ε(T) identifies distinct phase transitions transformation Figure 21, which occur at 240 K, 155 K and 145 K. In the high temperature (above 240 K) region the crystal structure is cubic and the organic cation is freely rotating within the inorganic cages formed by the $PbBr_6$ octahedra contributing significant to the dielectric permittivity at low frequencies. As the system is cooled down, the space group changes to tetragonal I (155-240 K) and the leading contribution to ε′ is the inorganic octahedra tilting out-of-phase, until the movement of the octahedra align to in-phase and transforms into the tetragonal II (145-155 K), while with even further decrease of the temperature (below 145K), the inorganic-organic compound freezes completely without any T-variation in the permittivity Figure 21.



[28]

Figure 20. Dielectric Spectroscopy of $MAPbBr_3$ frequency (Hz) , (500 Hz, 1 kHz, 10.15 kHz, 20.02 kHz, 30.02 kHz), vs Temperature (K) vs dielectric permittivity.

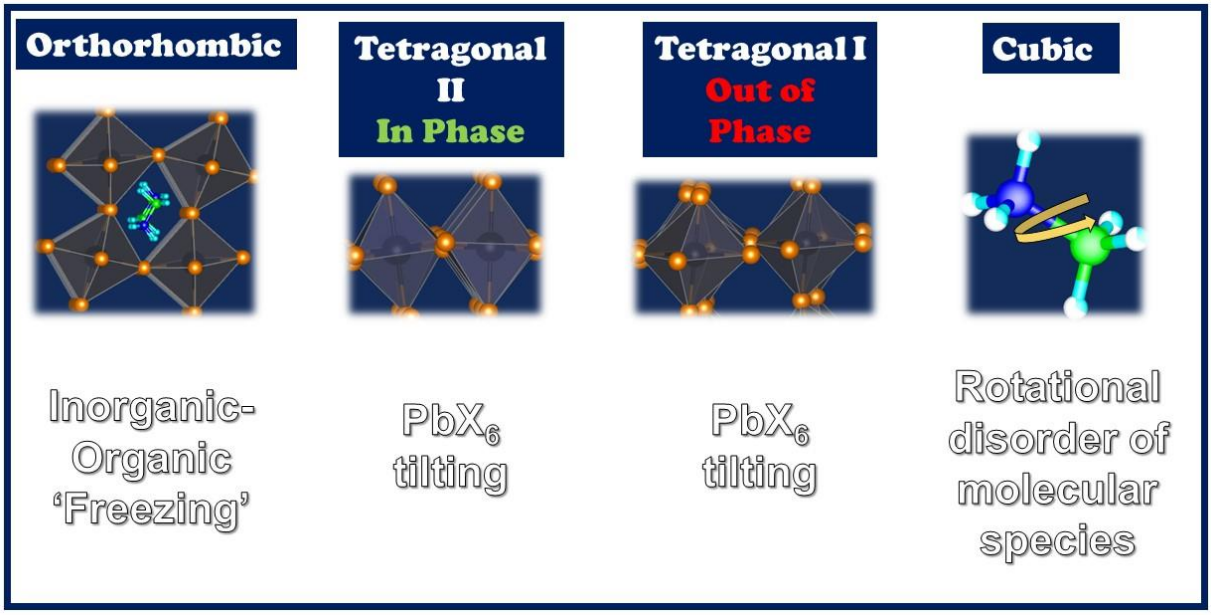


Figure 21. $MAPbBr_3$ crystal structure transformations.

In the case of $MAPbCl_3$ Figure. 22, ε(T) identifies distinct phase transitions transformation Figure. 23, which occurs at 178 K and 173 K. In the high temperature (320 K) region the crystal structure is cubic and the organic cation is freely rotating within the inorganic cages formed by the $PbCl_6$ octahedra contributing significant to the dielectric permittivity at low frequencies. As the system is cooled down, the space groups changes to tetragonal II (178 K) and the leading contribution to ε′ is the inorganic aligned in-phase motion of the octahedral, while with even further decrease of the temperature (below 173 K), the inorganic-organic compound freezes completely without any T-variation in the permittivity Figure 23.

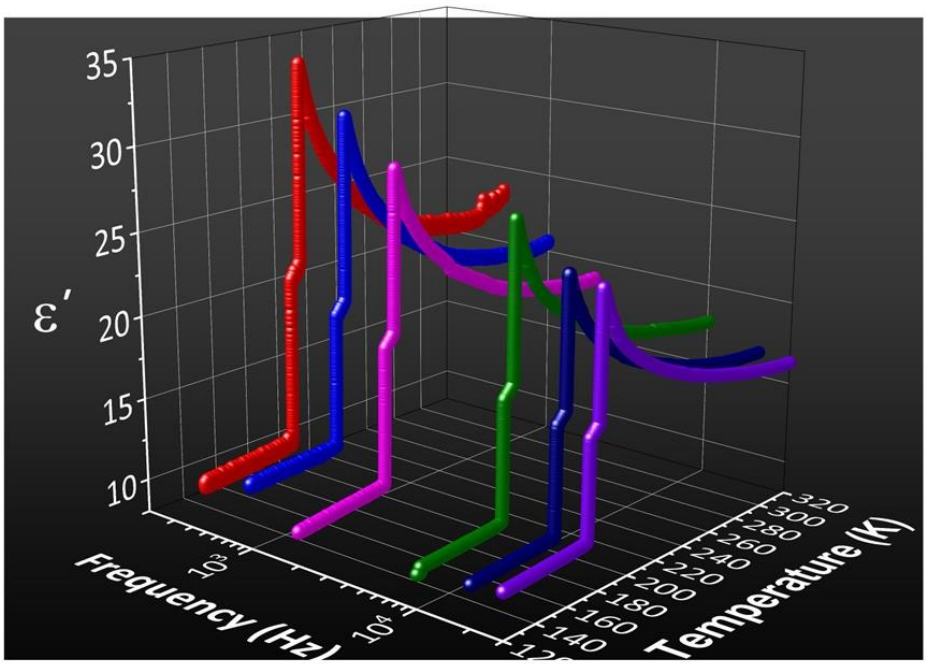


Figure 22. Dielectric Spectroscopy of $MAPbCl_3$ frequency (Hz), (500.1 Hz, 1.001 kHz, 2.001 kHz, 10.15 kHz, 20.02 kHz, 30.02 kHz), vs Temperature (K) vs dielectric permittivity.

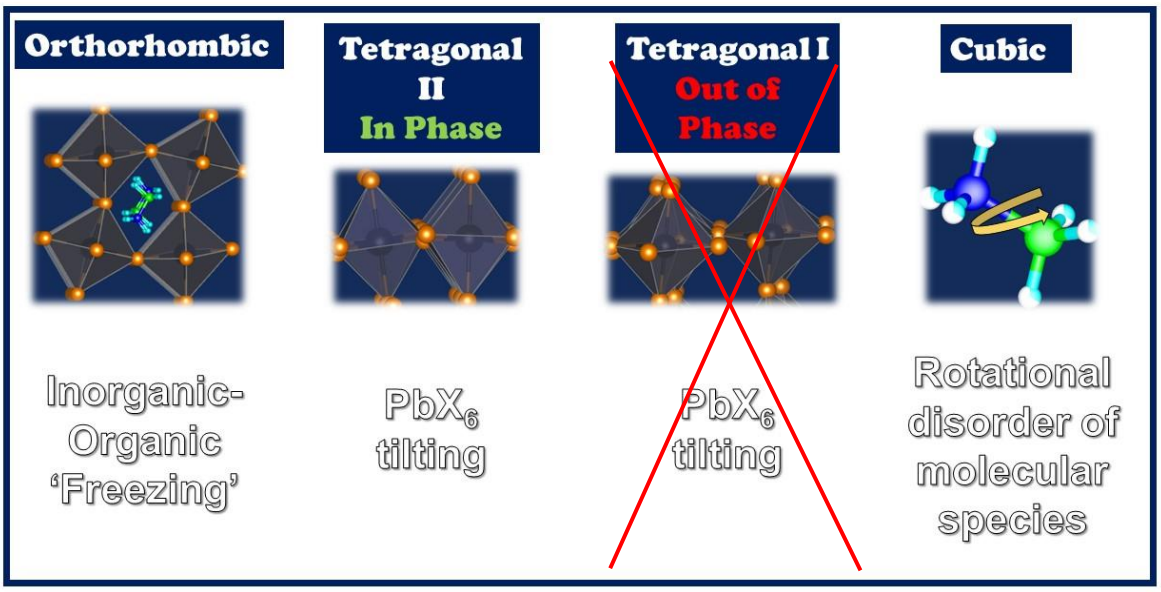


Figure 23. $MAPbCl_3$ crystal structure transformations.

3.Results and Discussion

3.1 Dielectric permittivity & Lattice Dynamics

The methylammonium lead bromide undergoes four phase transitions, from room temperature to 240 K from cubic ($Pm\bar{3}m$) it transforms to tetragonal I (I4/mcm), from 240 K to 155 K to tetragonal II (P4/mmm) and from 155 K to 145 K to orthorhombic ($Pna2_1$). In Figure. 24 a) we observe the dependence of the dielectric permittivity versus the temperature. Above the cubic phase transition, the significant dependance of the dielectric permittivity on the frequency corresponds to the motion of the organic cation, but at the lowest frequency 20 Hz the signal noise is enlarged due to the limit operation of the LCR Agilent E4980A. As we cool down at the tetragonal I region, we observe an increase of the dielectric permittivity, which appeared in first order transitions, following of a sharp drop down when entering the tetragonal II, and finally the dielectric permittivity is maintained constant, at the orthorhombic phase due to the freezing out of the organic cation and the locking up of the octahedral tilting, despite of an anomaly at 500 Hz.

The Figure 24 b) represents the Dissipation Factor versus the temperature, where for the low frequency of 20 Hz the signal noise is enhanced similarly to the real part of the permittivity as the LCR Agilent E4980A operate at the limit. At 500 Hz an anomaly behavior of the inhomogeneous charge of the sample occurs with a fluctuation of the dissipation factor. Increasing the frequency even further (1 kHz - 30.02 kHz) the dissipation decreases in the cubic structure (above 240K) corresponding the rotational motion of the organic cation. For the rest of the transitions, no observed any alteration due to the contribution of the inorganic lattice ($PbBr_6$ network of octahedral) is detected.

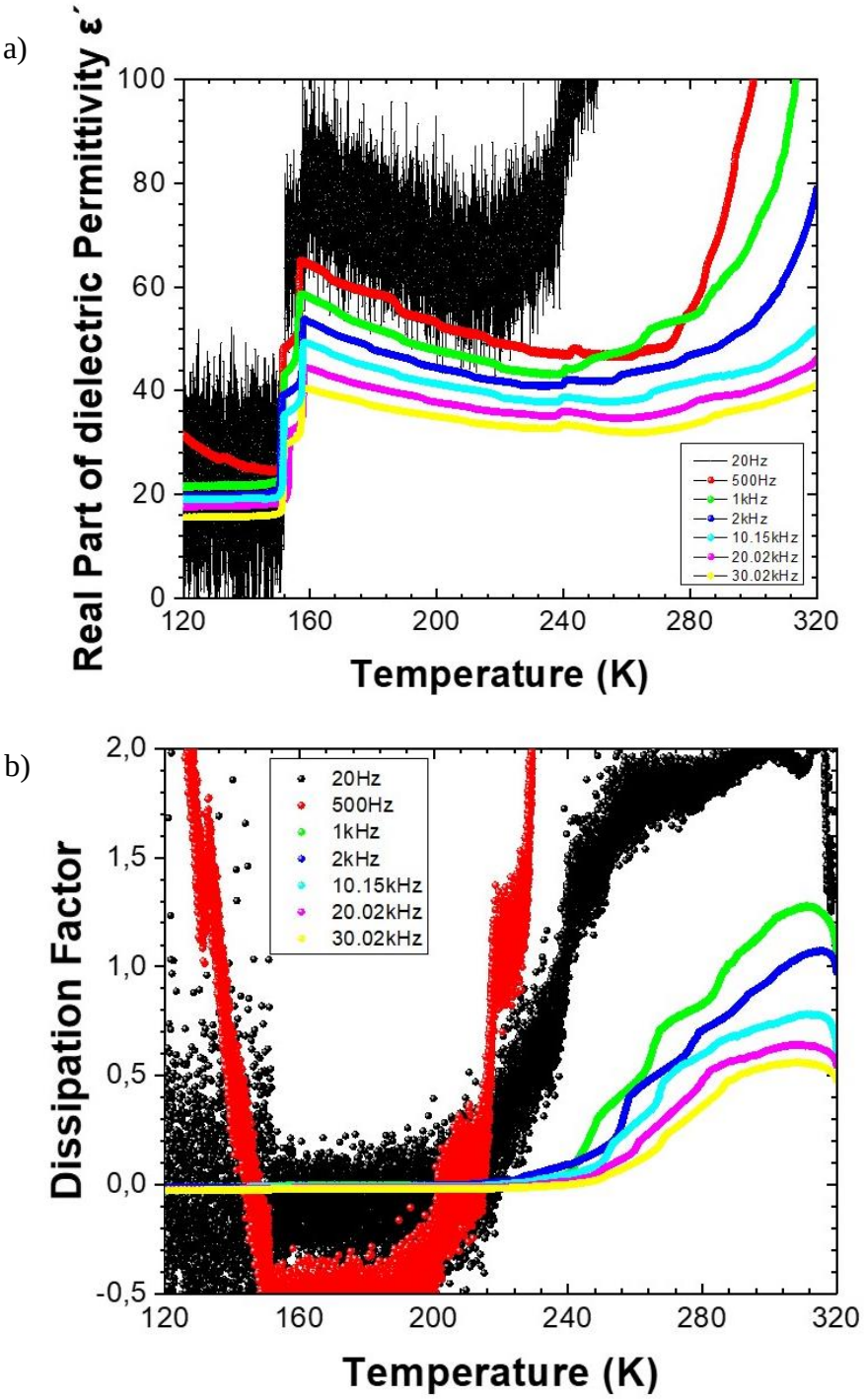
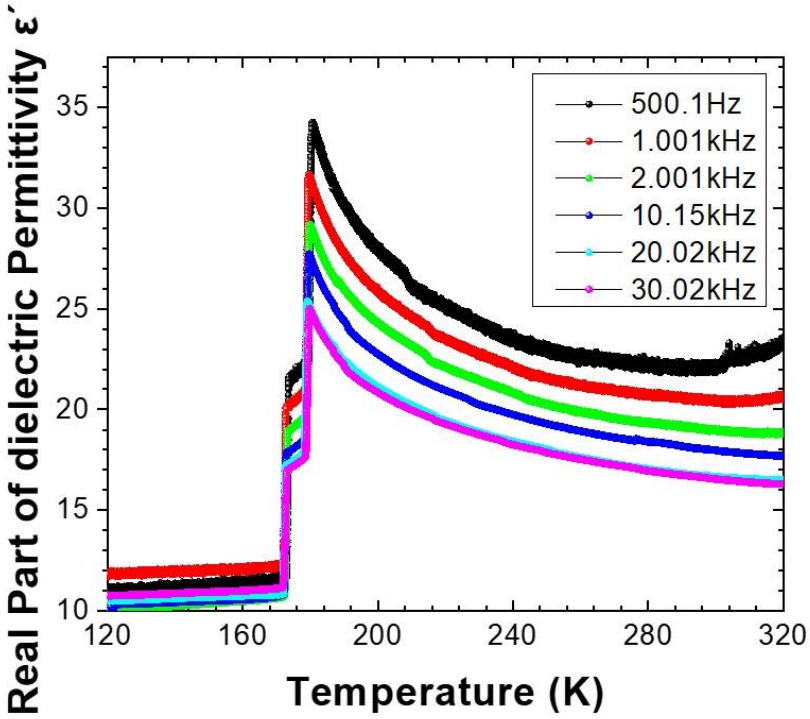


Figure 24. $MAPbBr_3$ temperature dependent dielectric measurements taken at different frequencies (20 Hz, 500 Hz, 1 kHz, 2 kHz, 10.15 kHz, 20.02 kHz, 30.02 kHz); (a) Dielectric Permittivity, (b) Dissipation Factor.

The methylammonium lead chloride undergoes four phase transitions, from room temperature to 178 K, from cubic ($Pm\bar{3}m$) it transforms to tetragonal II (P4/mmm) and at the range of 178 K to 173 K goes into the orthorhombic ($P222_1$). In this scenario, we avoided measuring the low frequencies (Hz region), except the 500.1 Hz, in order to avoid the noisy measurements. In Figure 25 a), we observe similar dependence of the dielectric permittivity versus the temperature to that met in the $MAPbBr_3$ analogue despite the different crystal structure transformations, while the magnitude of the dielectric permittivity was observed to be half of that in the bromide throughout the temperature region.

In the dissipation factor versus temperature plot, Figure. 25 b), the dissipation factor presents a similar behavior versus the frequency in the cubic (178 K) crystal structure, in this case the transformation of the tetragonal II (178 K) to orthorhombic (173 K) is detected at low frequencies (500.1 Hz, 1.001 kHz, 2.001kHz).

a)



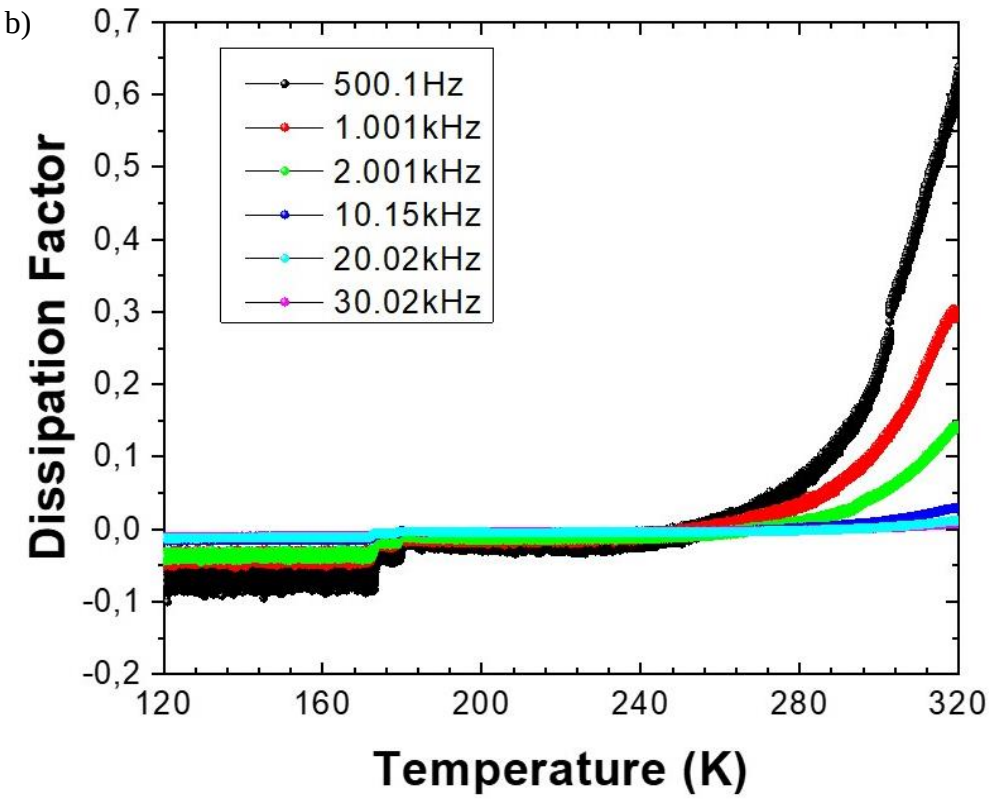


Figure 25. $MAPbCl_3$ temperature dependent dielectric measurements taken at different frequencies (500.1 Hz, 1.001 kHz, 2.001 kHz, 10.15 kHz, 20.02 kHz, 30.02 kHz); (a) Dielectric Permittivity, (b) Dissipation Factor.

3.2 Dielectric Properties Versus Frequency

In addition to the temperature dependent properties, the relaxation phenomena were studied by isothermal experiments and sweeping the frequency from 20 Hz to 2 MHz, with a delay of 20 sec at each measured point and an initial 600 sec delay to charge electrically the sample fully. All the measurements were applied in heating process, with a rate of 0.5 K/min from 120-320 K choosing different temperatures to investigate the behavior corresponding to the different structural phases involved in each perovskite by utilizing the LCR Agilent E4980A, with an electric field stimulation of 1 kV/m for the $MAPbBr_3$ and 0.5 kV/m for the $MAPbCl_3$.

In the case of $MAPbBr_3$ we choose to measure the frequency dependence of the permittivity at two temperatures in the region of each possible structural phase transition. In the orthorhombic phase (below 155 K) we measured at 120 K and 140 K, in the tetragonal II (145-155 K) we avoided to measure due to the small window of the temperature, but in the tetragonal I (155-240 K) we measured at 180 K and 220 K, while for the cubic (above 240 K), we measured at 260 K and 300 K.

In Figure 26 a) we observe the real part of the dielectric permittivity ε′ versus the frequency in the chosen temperatures. In the orthorhombic and tetragonal phases, the dielectric permittivity is independent from the frequency expect in the higher symmetry (300 K, cubic structure), the permittivity decreases until 10 kHz and makes a plateau. The imaginary part of dielectric permittivity ε′′ Figure. 26 b) presents an anomaly as the frequency increases, the ε′′ decreases with a significant rate resulting to the decreased dielectric losses. The real part of electrical Modulus M′ Figure. 26 c) presents relaxation phenomena in the high symmetry (300 K cubic crystals structure) until 10 kHz. For the low temperatures (120 K and 140 K), we observe noisy measurements in the low frequency region (20 Hz to $2 \cdot 10^2$ Hz). In Figure. 26 d), the electrical modulus M′′ is increased with the increasing of the frequency which is also dependent to the temperature. The maximum M′′ is shifted in higher frequencies with the increase of the temperature.

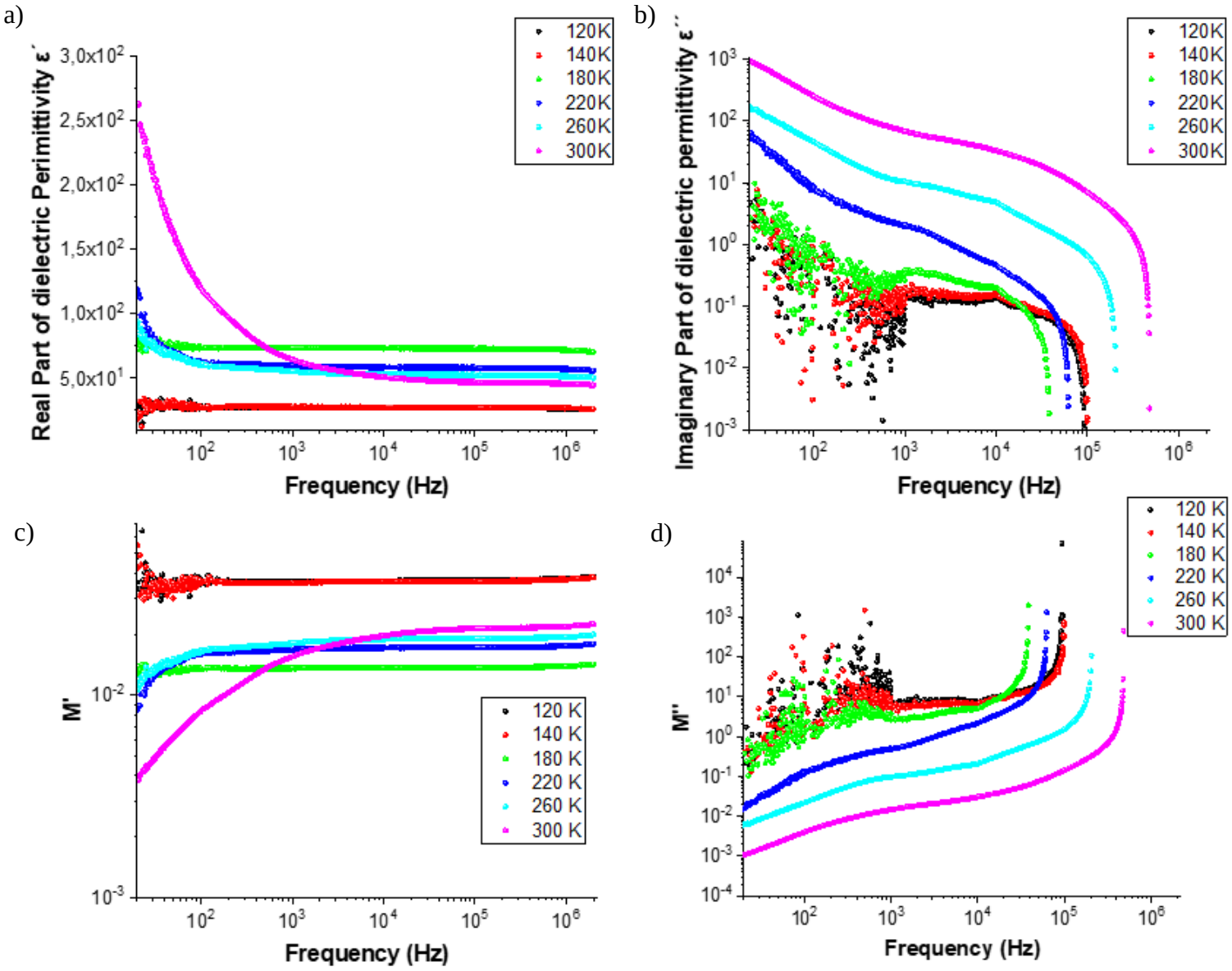


Figure 26. Isothermal, frequency dependent (20 Hz to 2 MHz) dielectric permittivity experiments of the $MAPbBr_3$, (a) real part of the dielectric permittivity ε´, (b) imaginary part of the dielectric permittivity ε´´, (c) Real part of the electrical Modulus, M´, (d) Imaginary part of the electrical Modulus, M´´.

In the case of $MAPbCl_3$, a similar experiment was conducted at 130 K and 160 K (orthorhombic), 175 K (tetragonal II) and at the cubic (190 K, 240 K, 280 K, 320 K) crystal structures.

In Figure 27 a) we observe that the dependency of the dielectric permittivity affects only the high symmetry (cubic phase) similarly to the $MAPbBr_3$. In the case of the imaginary part Figure. 27 b) the same decreasing anomaly is observed with reduced rate than that observed in $MAPbBr_3$. The real part of electrical Modulus M´ Figure. 27 c) also presents a strong dependence to temperature and an anomaly at 175 K in the frequency range of 10^5 -10^6 Hz. In Figure 27 d) the imaginary part of the electrical Modulus M´´ represents the maximum of the M´´ at higher frequencies as the LCR provide.

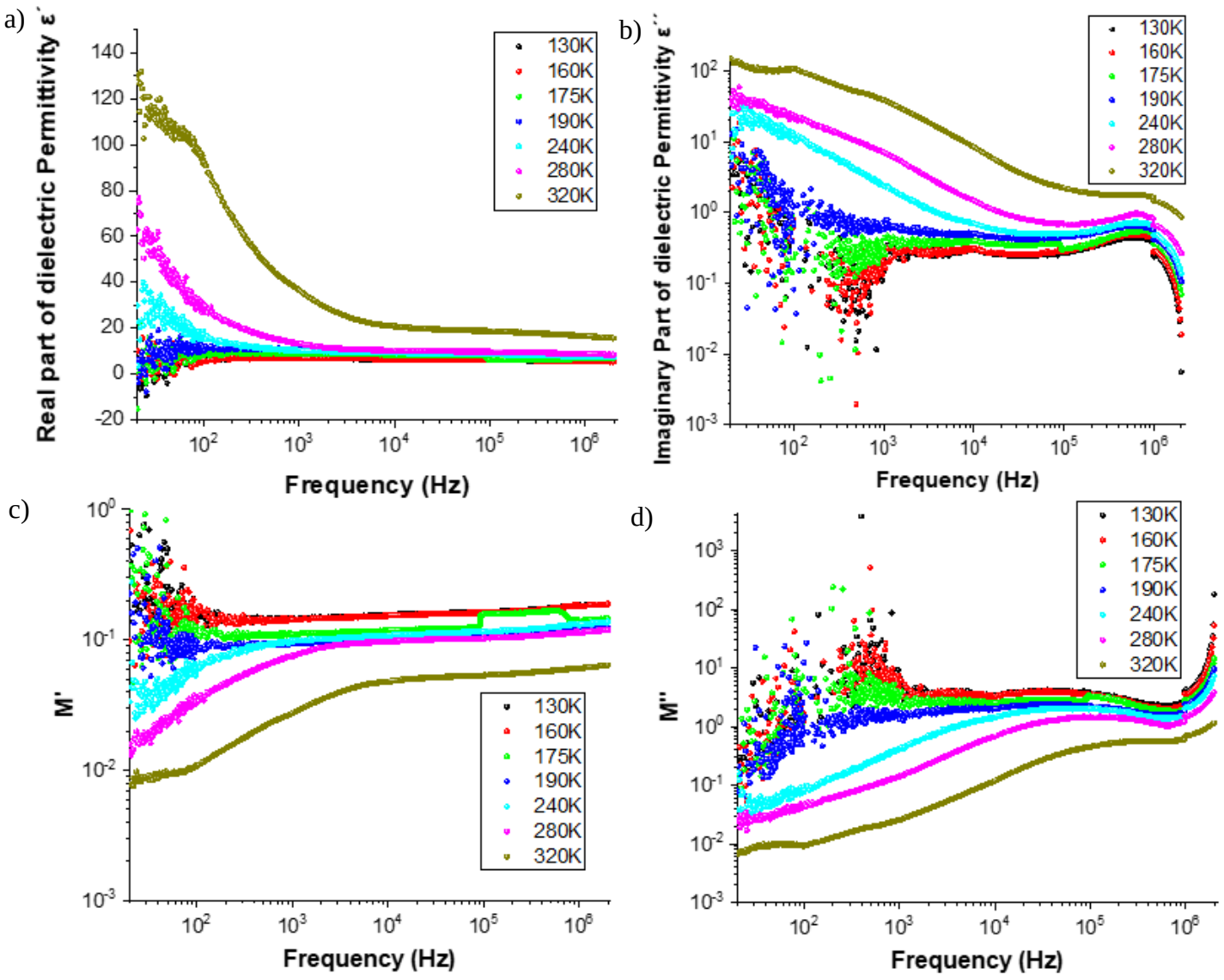


Figure 27. Isothermal, frequency dependent (20 Hz to 2 MHz) dielectric permittivity experiments of the $MAPbCl_3$, (a) real part of the dielectric permittivity ε′, (b) imaginary part of the dielectric permittivity ε′′, (c) Real part of the electrical Modulus, M′, (d) Imaginary part of the electrical Modulus, M′′.

4.Analysis

Following the isothermal experiments, we attempt to analyse the relaxation behaviours withn the 20 Hz to 10^5 Hz frequency range, at the high temperature region, using the four different relaxations models involving the real part of the dielectric permittivity, which were introduced in the Dielectric & Optoelectronic Properties chapter (eq. 8, 10, 11, 12).

In the case of $MAPbBr_3$ Figure. 28, initialy keep constant the ε_∞= 45.45 (was chosen at 10^5 Hz due to the observasion of the plato after the decrease of the dielectric permittivity) and ε_s=252 (was chosen at 20 Hz due assumation of a palto before the decrease of the permittivity) in all models and we attempt to fit the data with all four mathematical expressions (eq. 8, 10, 11, 12). Initialy by fitting the Debye model we calculated the relaxation time as τ = 0.01518(2) sec. Moving in the next model, namely, the Cole-Cole we calculated the relaxation time as τ = 0.01370(9) sec and the exponent α = 0.21872(7), which represents stretching of dipoles. On the basis of the Cole-Davidson model we calculated the relaxation time as τ = 0.01370(9) sec and the exponent β = 0.80574(4), which indicates the relation of the relaxation mechanism with the temperature. As for the Harvliak-Negami model, the fitting to the experimental data appears as optimal, with with relaxation time calculated as τ = 0.0271(4), while the parameters α and β were fixed to values acquired from previous model prediction. Calculating initialy the relaxation time τ = 0.02706(4) sec, and after that we recalculate the parameters a and b resulting α= 0.21872(7), (same as the previous model Cole-Cole), and β= 0.51922(2). All the parameters are compiled in Table 1. The parameters α and β may suggest that the dipoles are steched and also some degree of relaxation due to temperature agitation may also be in place.

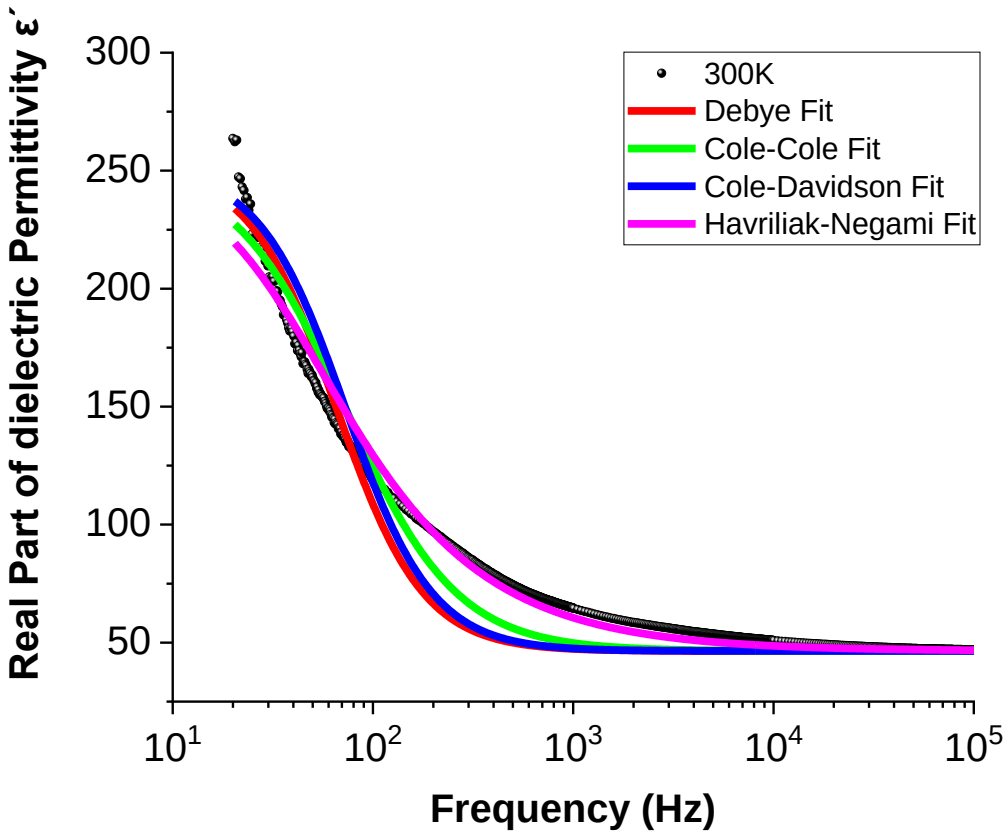


Figure 28. Assessing different ε(ω) relaxation models (eq. 8 to 11) against the $MAPbBr_3$ data.

	τ (sec)	**α**	**β**
Debye	0.01518(2)	-	-
Cole-Cole	0.01370(9)	0.21872(7)	-
Cole-Davidson	0.01370(9)	-	0.80574(4)
Havriliak-Negami	0.02706(4)	0.21872(7)	0.51922(2)

Table 1. Calculated ralaxation parameters of $MAPbBr_3$ at 300K on the basis of various relaxation models.

In the case of $MAPbrCl_3$ Figure. 29, initialy keep constant the ε_∞= 18.7 (was chosen at 10^5 Hz due to the observasion of the plato after the decrease of the dielectric permittivity) and ε_s=113 (was chosen at 20 Hz due to the observation of a palto before the decrease of the permittivity) in all models and we attempt to fit the data with all four mathematical expressions (eq. 8, 10, 11, 12). Initialy by fitting the Debye model we calculated the relaxation time as τ = 0.00367(5) sec. Moving in the next model, namely, the Cole-Cole we fix relaxation time as τ = 0.00367(5) sec (relaing on the previus model) and the exponent α = 0.267(7), which represents stretching of dipoles. On the basis of the Cole-Davidson model we calculated the relaxation time as τ = 0.00570(3) sec and the exponent β = 0.58801(4), which indicates the relation of the relaxation mechanism with the temperature. As for the Harvliak-Negami model, the fitting to the experimental data appears as optimal, with with relaxation time calculated as τ = 0.00653(6) sec, while the parameters α and β were fixed to values acquired from previous model prediction. All the parameters are compiled in Table 2. The parameters α and β may suggest that the dipoles are steched and also some degree of relaxation due to temperature agitation may also be in place.

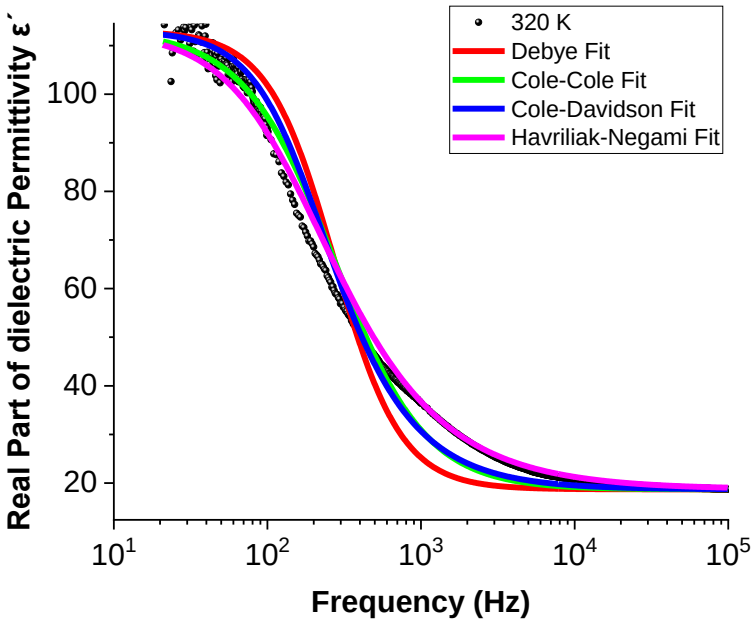


Figure 29. Assessing different $\varepsilon(\omega)$ relaxation models (eq. 8 to 11) against the $MAPbCl_3$ data.

	τ (sec)	α	β
Debye	0.00367(5)	-	-
Cole-Cole	0.00367(5)	0.267(7)	-
Cole-Davidson	0.00570(3)	-	0.58801(4)
Havriliak-Negami	0.00653(6)	0.267(7)	0.58801(4)

Table 2. Calculated ralaxation parameters of $MAPbCl_3$ at 320K on the basis of different relaxation models.

Following the literature the $MAPbX_3$ (Cl^- , Br^-) have been studied via dielectric spectroscopy initially 1987 by A. Poglitsch and D. Weber [27] within a wider frequency range (GHz) studying the temperature dependence of the halide perovskites and predicted the dipole relaxation due to an anomaly of the imaginary part of the imaginary part of the dielectric permittivity in the 50 GHz. Since then, better crystal growth techniques have been proposed providing single crystals of better quality and also better scientific tools as the LCR with better accuracy. Damjanovic et. al [28] were the first who attempted to introduce the Debye models for the $MAPbBr_3$ with the isothermal experiment and infer the mismatch of the imaginary part into the fitting model and suggest a high level of disorder in the $MAPbX_3$ crystals.

The aforementioned analysis suggests that the best fitted model may be the Havriliak-Negami for both systems. With the values of exponents α and β being relatively close to each other, this may be due to the nature of very same organic cation that is responsible for the relaxation mechanism. As for the relaxation time, in the case of the bromide the τ is four times the τ of the chloride. This may be contributed to the size of the octahedral hole (size of the octahedral hole $0.41r_x$/Å) [29]. As for the Chloride it is 0.76 and for the Bromide it is 0.80. Resulting the bigger cavities for the means more ‘’free space’’ for the organic cation to rotate.

5.Conclusions and Perspective

Single crystals of the hybrid $CH_3NH_3PbBr_3$ and $CH_3NH_3PbCl_3$ were grown using the inverse temperature crystallization technique. The crystals were structurally and spectroscopically characterized to validate their phase purity and optical quality for optoelectronics. The structure dynamic of the halide perovskites was studied with the correlation of the dielectric permittivity to the temperature. The relaxation mechanisms were introduced via isothermal procedures by ramping the frequency of the AC electric field. The Havriliak-Negami model appears as optimal fit, providing information about the dependence of the relaxation mechanism to the temperature and the stretched shape of the dipoles.

Future work concerns the dielectric study with higher frequency range to prove the relation of the imaginary part (the gaussian behavior) of the $MAPbCl_3$ and $MAPbBr_3$ in the GHz region. The calculation of the relaxation time and the exponents α, β, for different organic cation. Investigate the dielectric properties of possible two-dimensional candidates.

6.Literature

(1) Front Matter. In *Perovskite Materials for Energy and Environmental Applications*; Ahmad, K., Raza, W., Eds.; Wiley, 2022. https://doi.org/10.1002/9781119763376.fmatter.

(2) Peña, M. A.; Fierro, J. L. G. Chemical Structures and Performance of Perovskite Oxides. *Chem. Rev.* **2001**, *101* (7), 1981–2018. https://doi.org/10.1021/cr980129f.

(3) Wells, H. L. Über Die Cäsium- Und Kalium-Bleihalogenide. *Z. Anorg. Chem.* **1893**, *3* (1), 195–210. https://doi.org/10.1002/zaac.18930030124.

(4) Weber, D. CH3NH3SnBrxl3 x (x = 0 - 3) , ein Sn(II)-System mit kubischer Perowskitstruktur. 4.

(5) Stoumpos, C. C.; Malliakas, C. D.; Kanatzidis, M. G. Semiconducting Tin and Lead Iodide Perovskites with Organic Cations: Phase Transitions, High Mobilities, and Near-Infrared Photoluminescent Properties. *Inorg. Chem.* **2013**, *52* (15), 9019–9038. https://doi.org/10.1021/ic401215x.

(6) Mitzi, D. B.; Liang, K.; Wang, S. Synthesis and Characterization of [NH $_2$ C(I)NH $_2$] $_2$ ASnI $_5$ with A = Iodoformamidinium or Formamidinium: The Chemistry of Cyanamide and Tin(II) Iodide in Concentrated Aqueous Hydriodic Acid Solutions. *Inorg. Chem.* **1998**, *37* (2), 321–327. https://doi.org/10.1021/ic971332g.

(7) Kojima, A.; Teshima, K.; Shirai, Y.; Miyasaka, T. Organometal Halide Perovskites as Visible-Light Sensitizers for Photovoltaic Cells. *J. Am. Chem. Soc.* **2009**, *131* (17), 6050–6051. https://doi.org/10.1021/ja809598r.

(8) Green, M.; Dunlop, E.; Hohl-Ebinger, J.; Yoshita, M.; Kopidakis, N.; Hao, X. Solar Cell Efficiency Tables (Version 57). *Prog Photovolt Res Appl* **2021**, *29* (1), 3–15. https://doi.org/10.1002/pip.3371.

(9) Johnsson, M.; Lemmens, P. Crystallography and Chemistry of Perovskites. In *Handbook of Magnetism and Advanced Magnetic Materials*; Kronmüller, H., Parkin, S., Eds.; John Wiley & Sons, Ltd: Chichester, UK, 2007; p 411. https://doi.org/10.1002/9780470022184.hmm411.

(10) Gholipour, S.; Saliba, M. Bandgap Tuning and Compositional Exchange for Lead Halide Perovskite Materials. In *Characterization Techniques for Perovskite Solar Cell Materials*; Elsevier, 2020; pp 1–22. https://doi.org/10.1016/B978-0-12-814727-6.00001-3.

(11) Govinda, S.; Kore, B. P.; Bokdam, M.; Mahale, P.; Kumar, A.; Pal, S.; Bhattacharyya, B.; Lahnsteiner, J.; Kresse, G.; Franchini, C.; Pandey, A.; Sarma, D. D. Behavior of Methylammonium Dipoles in MAPbX $_3$ (X = Br and I). *J. Phys. Chem. Lett.* **2017**, *8* (17), 4113–4121. https://doi.org/10.1021/acs.jpclett.7b01740.

(12) Ichikawa, M.; Gustafsson, T.; Olovsson, I. Is NaNO2 a Pure Order–Disorder Type Ferroelectric? *Solid State Communications* **2002**, *123* (3–4), 135–139. https://doi.org/10.1016/S0038-1098(02)00207-7.

(13) Acosta, M.; Novak, N.; Rojas, V.; Patel, S.; Vaish, R.; Koruza, J.; Rossetti, G. A.; Rödel, J. BaTiO $_3$ -Based Piezoelectrics: Fundamentals, Current Status, and

Perspectives. *Applied Physics Reviews* **2017**, *4* (4), 041305. https://doi.org/10.1063/1.4990046.

(14) Eleni Aza, (2019), Strongly correlated Transition Metal Oxides: Synthesis, Structure, Magnetic, Dielectric and Dynamical properties, PhD thesis.

(15) Han, X.-B.; Chai, C.-Y.; Liang, B.-D.; Fan, C.-C.; Zhang, W. Ferroic Phase Transition Molecular Crystals. *CrystEngComm* **2022**, *24* (8), 1507–1517. https://doi.org/10.1039/D2CE00009A.

(16) Ali, F.; Zhou, D.; Sun, N.; Ali, H. W.; Abbas, A.; Iqbal, F.; Dong, F.; Kim, K.-H. Fluorite-Structured Ferroelectric-/Antiferroelectric-Based Electrostatic Nanocapacitors for Energy Storage Applications. *ACS Appl. Energy Mater.* **2020**, *3* (7), 6036–6055. https://doi.org/10.1021/acsaem.0c00987.

(17) Younsi, K.; Neti, P.; Shah, M.; Zhou, J.; Krahn, J.; Weeber, K.; Whitefield, C. On-Line Capacitance and Dissipation Factor Monitoring of AC Stator Insulation. *IEEE Trans. Dielect. Electr. Insul.* **2010**, *17* (5), 1441–1452. https://doi.org/10.1109/TDEI.2010.5595545.

(18) Coşkun, M.; Polat, Ö.; Coşkun, F. M.; Durmuş, Z.; Çağlar, M.; Türüt, A. The Electrical Modulus and Other Dielectric Properties by the Impedance Spectroscopy of $LaCrO_3$ and $LaCr_{0.90}Ir_{0.10}O_3$ Perovskites. *RSC Adv.* **2018**, *8* (9), 4634–4648. https://doi.org/10.1039/C7RA13261A.

(19) Herz, L. M. How Lattice Dynamics Moderate the Electronic Properties of Metal-Halide Perovskites. *J. Phys. Chem. Lett.* **2018**, *9* (23), 6853–6863. https://doi.org/10.1021/acs.jpclett.8b02811.

(20) Davidson, D. W.; Cole, R. H. Dielectric Relaxation in Glycerol, Propylene Glycol, and *n* -Propanol. *The Journal of Chemical Physics* **1951**, *19* (12), 1484–1490. https://doi.org/10.1063/1.1748105.

(21) Zhang, Z.; Zhang, Z.; Hao, B. N.; Zhang, H.; Wang, M.; Liu, Y. D. Fabrication of Imidazolium-Based Poly(Ionic Liquid) Microspheres and Their Electrorheological Responses. *J Mater Sci* **2017**, *52* (10), 5778–5787. https://doi.org/10.1007/s10853-017-0812-4.

(22) Saidaminov, M. I.; Abdelhady, A. L.; Murali, B.; Alarousu, E.; Burlakov, V. M.; Peng, W.; Dursun, I.; Wang, L.; He, Y.; Maculan, G.; Goriely, A.; Wu, T.; Mohammed, O. F.; Bakr, O. M. High-Quality Bulk Hybrid Perovskite Single Crystals within Minutes by Inverse Temperature Crystallization. *Nat Commun* **2015**, *6* (1), 7586. https://doi.org/10.1038/ncomms8586.

(23) Petříček, V.; Dušek, M.; Palatinus, L. Crystallographic Computing System JANA2006: General Features. *Zeitschrift für Kristallographie - Crystalline Materials* **2014**, *229* (5), 345–352. https://doi.org/10.1515/zkri-2014-1737.

(24) Maculan, G.; Sheikh, A. D.; Abdelhady, A. L.; Saidaminov, M. I.; Haque, M. A.; Murali, B.; Alarousu, E.; Mohammed, O. F.; Wu, T.; Bakr, O. M. $CH_3NH_3PbCl_3$ Single Crystals: Inverse Temperature Crystallization and Visible-Blind UV-Photodetector. *J. Phys. Chem. Lett.* **2015**, *6* (19), 3781–3786. https://doi.org/10.1021/acs.jpclett.5b01666.

(25) Ding, J.; Zhao, Y.; Du, S.; Sun, Y.; Cui, H.; Zhan, X.; Cheng, X.; Jing, L. Controlled Growth of MAPbBr3 Single Crystal: Understanding the Growth Morphologies of Vicinal Hillocks on (100) Facet to Form Perfect Cubes. *J Mater Sci* **2017**, *52* (13), 7907–7916. https://doi.org/10.1007/s10853-017-0995-8.
(26) Yang, L.; Kruse, B. Revised Kubelka–Munk Theory I Theory and Application. *J. Opt. Soc. Am. A* **2004**, *21* (10), 1933. https://doi.org/10.1364/JOSAA.21.001933.
27) Poglitsch, A.; Weber, D. Dynamic Disorder in Methylammoniumtrihalogenoplumbates (II) Observed by Millimeter-wave Spectroscopy. *The Journal of Chemical Physics* **1987**, *87* (11), 6373–6378. https://doi.org/10.1063/1.453467.
(28) Vasiljevic, M.; Kollár, M.; Spirito, D.; Riemer, L.; Forró, L.; Horváth, E.; Gorfman, S.; Damjanovic, D. "Forbidden" Polarisation and Extraordinary Piezoelectric Effect in Organometallic Lead Halide Perovskites. *Adv Funct Materials* **2022**, 2204898. https://doi.org/10.1002/adfm.202204898.
(29) W. Travis, E. N. K. Glover, H. Bronstein, D. O. Scanlon, and R. G. Palgrave, *On the Application of the Tolerance Factor to Inorganic and Hybrid Halide Perovskites:*

A Revised System, Chem. Sci. **7**, 4548 (2016).

https://doi.org/10.1039/C5SC04845A.